Birnessite polytype systematics and identification by powder X-ray diffraction

Victor.A. Drits, Bruno Lanson, Anne-Claire Gaillot

Birnessite polytype systematics and identification by powder X-ray diffraction

Revision 1

Victor A. Drits[1, 2]

Bruno Lanson[1,*]

Anne-Claire Gaillot[1]

1 – Environmental Geochemistry Group, LGIT – Maison des Géosciences, University of Grenoble – CNRS, 38041 Grenoble Cedex 9, France.

2 – Geological Institute, Russian Academy of Sciences, 7 Pyzhevsky street, 109017 Moscow, Russia

* Author to whom correspondence should be addressed.

e-mail: Bruno.Lanson@obs.ujf-grenoble.fr

ABSTRACT

The polytypes of birnessite with a periodic stacking along the **c*** axis of one-, two-, and three-layers are derived in terms of an anion close-packing formalism. Birnessite layers may be stacked so as to build two types of interlayers: P-type in which basal O atoms from adjacent layers coincide in projection along the **c*** axis, thus forming interlayer prisms; and, O-type in which these O atoms form interlayer octahedra. The polytypes can be categorized into three groups that depend on the type of interlayers: polytypes consisting of homogeneous interlayers of O- or P-type, and polytypes in which both interlayer types alternate. Ideal birnessite layers can be described by a hexagonal unit-cell ($a_h = b_h \approx 2.85$ Å and $\gamma = 120°$) or by an orthogonal C-centered cell ($a = \sqrt{3}\, b$, $b_h \approx 2.85$ Å and $\gamma = 90°$); and, hexagonal birnessite polytypes ($1H$, $2H_1$, $2H_2$, $3R_1$, $3R_2$, $3H_1$, and $3H_2$) have orthogonal analogues ($1O$, $2O_1$, $2O_2$, $1M_1$, $1M_2$, $3O_1$, and $3O_2$).

X-ray diffraction (XRD) patterns from different polytypes having the same layer symmetry and the same number of layers per unit cell exhibit *hkl* reflections at identical 2θ positions. XRD patterns corresponding to such polytypes differ only by their *hkl* intensity distributions, thus leading to possible ambiguities in polytype identification. In addition, the characteristics of the birnessite XRD patterns depends not only on the layer stacking but also on the presence of vacant layer sites, and on the type, location and local environment of interlayer cations.

Several structure models are described for birnessite consisting of orthogonal vacancy-free or of hexagonal vacancy-bearing layers. These models differ by their stacking modes and by their interlayer structures, which contain mono-, di-, or tri-valent cations. Calculated XRD patterns for these models show that the *hkl* intensity distributions are determined by the polytype, with limited influence of the interlayer structure. Actual structures of

phyllomanganates can thus be approximated by idealized models for polytype identification purpose. General rules for this identification are formulated. Finally, the occurrence of the different polytypes among natural and synthetic birnessite described in the literature is considered with special attention given to poorly understood structural and crystal-chemical features.

INTRODUCTION

Birnessite is a hydrous layered manganese oxide (phyllomanganate). Its layers consist of edge-sharing MnO_6 octahedra and these layers are separated from each other by hydrated interlayer cations. These cations compensate for a layer charge deficit arising either from the presence of vacant layer sites or from the coexistence of heterovalent Mn cations in the octahedral layer. Birnessite interlayers incorporate a single sheet of interlayer H_2O molecules, and exhibit a minimum periodicity along the **c*** axis of ~7 Å (Giovanoli et al. 1970a, 1970b; Burns and Burns 1977; Chukhrov et al. 1978; Post and Veblen 1990). In the following the term "birnessite" will be used to describe all natural and synthetic materials with such a layer structure, whatever the origin of the layer charge, and the actual configuration and chemical composition of the interlayers.

Over the last few decades, birnessite has attracted a wide interest for several reasons. First, it is ubiquitous in geological environments in spite of the low abundance of Mn. It is for example a major component of Mn nodules, which cover huge areas of the ocean floor and the bottom of some lakes. It is also present in soils, sediments, and Mn-rich ore deposits (Burns and Burns 1977, 1978; Chukhrov et al. 1978, 1985; Drits et al. 1985; Golden et al. 1986; Cornell and Giovanoli 1988; Manceau et al. 2000c). It was recently shown that bacteria play a major role in the formation of birnessite in most of these environments (Tebo and He 1999; Tebo et al. 2004; and references therein). Second, this mineral plays an essential role in different ion-exchange and redox processes because of its unique surface charge, and adsorption and redox properties (Manceau and Charlet 1992; Manceau et al. 1992a, 1992b; Paterson et al. 1994; Stone et al. 1994; Tu et al. 1994; Le Goff et al. 1996; Silvester et al. 1997). In particular, birnessite plays a pivotal role in the fate of heavy metals and other pollutants in contaminated water systems and soils (Chao and Theobald 1976; Manceau et al.

1997, 1999, 2000a, 2000b). Despite its low concentration, birnessite controls the distribution of some trace elements such as radionuclides, Pt-group elements, and rare earth elements (Manceau et al. 1999). In addition, birnessite has also attracted special attention because of its potential use as materials for batteries and other industrial applications (Kim et al. 1999).

Third, birnessite can be synthesized under a variety of physico-chemical conditions and from 0 to 1000°C. Synthetic birnessite is used to mimic naturally occurring redox and adsorption processes, being considered as analogous to natural varieties. Birnessite can be synthesized by the oxidation of Mn^{2+} in a highly alkaline medium (Giovanoli et al. 1970a, 1970b; Cornell and Giovanoli 1988; Kim et al. 2000), leading, for example, to the topotactic transformation of $Mn(OH)_2$ when subjected to the action of different oxidizers. Other methods using MnO_4^- as starting reagent (Herbstein et al. 1971; Ching et al. 1995, 1997a, 1997b; Chen et al. 1996a, 1996b; Ching and Suib 1997; Kim et al. 1999) include mild hydrothermal syntheses (Feng et al. 1995; Chen et al. 1996a, 1996b), sol-gel processes (Bach et al. 1990, 1993; Le Goff et al. 1994; Ching et al. 1995, 1997a; Cho et al. 1999), interactions of $KMnO_4$ with hydrochloric acid, and ion-exchange of the hydrogen form of birnessite to the Na- or K-forms (Tsuji et al. 1992; Leroux et al. 1995), and thermal decomposition of $KMnO_4$ at high temperature (Kim et al. 1999).

These different methods lead to the crystallization of birnessite having different layer stackings and different interlayer structures, which depend on the chemical nature of interlayer cations, their amounts, distribution, and coordination geometry. In addition birnessite is, as a rule, fine-grained and contains stacking faults and/or consists of interstratified layer types corresponding to different birnessite polytypes (Drits et al. 1997a, 2002; Silvester et al. 1997; Manceau et al. 2000c, 2002; Lanson et al. 2002a, 2002b). As a result, strikingly different X-ray diffraction patterns are obtained from birnessite crystallized under different physico-chemical conditions. As a consequence, there has been a lot of

98 confusion, even in the recent literature, as to the structure of these layer manganates (e.g.,
99 Chen et al. 1996b; Kim et al. 1999; Yang and Wang 2001). One difficulty in the interpretation
100 of the birnessite XRD patterns is that until recently even unit-cell parameters reported in the
101 literature were not determined unambiguously. Therefore, determination of birnessite
102 structure was sometimes limited to a general description of the XRD patterns without any
103 indexing or accurate determination of the unit-cell parameters (Feng et al. 1997a, 1997b;
104 Aronson et al. 1999; Ma et al. 1999; Yang and Wang 2001). In some cases indexing of *hkl*
105 reflections was carried out without proper justification (e.g., Le Goff et al. 1994, 1996; Ching
106 et al. 1995; Aronson et al. 1999). Significant progress was achieved recently in the structural
107 characterization of birnessite (Post and Veblen 1990; Kuma et al. 1994; Drits et al. 1997a,
108 1998, 2002; Manceau et al. 1997, 2000c, 2002; Silvester et al. 1997; Lanson et al. 2000,
109 2002a, 2002b) and specifically in the determination of their unit-cell parameters (Chen et al.
110 1996a, 1996b; Kim et al. 1999; Lanson et al. 2000, 2002a, 2002b). However, no systematic
111 description of reliable criteria for the identification of birnessite polytypes is available, to our
112 knowledge, in existing literature.

113 As for layer silicates (Bailey 1988) the optimal way to establish such criteria is to
114 deduce theoretically all birnessite polytypes taking into account the main crystal chemical
115 features of their layers and interlayers, to calculate the corresponding XRD patterns and to
116 formulate diffraction criteria for their identification. This paper is devoted to such a
117 systematic approach and describes how birnessite polytypes having the same unit-cell
118 parameters can be identified.

119

120 **BIRNESSITE POLYTYPE DIVERSITY**

121

Polytype diversity in terms of close-packing formalism

The two-dimensional periodicity of birnessite layers can be described either by a hexagonal unit-cell, with $a_h = b_h \approx 2.85$ Å and $\gamma = 120°$, or by an equivalent orthogonal C-centered cell, with $a = \sqrt{3}\, b$, $b_h \approx 2.85$ Å and $\gamma = 90°$. The orthogonal C-centered cell will be used systematically throughout the current manuscript. The birnessite layer consists of two closely packed anion sheets "sandwiching" Mn cations. The anion close-packing formalism can thus be used to describe the mutual arrangement of birnessite layers. As a first step all possible periodic stackings of birnessite layers with periodicity along the **c** axis of 1, 2, and 3 layers will be considered. Non-equivalent crystallographic sites of the layer oxygen atoms (O_{layer}) will be hereafter described with capital letters A, B, and C, whereas positions of the Mn cations will be described with corresponding a, b and c letters (Fig. 1). It is systematically assumed that the lower surface of the first birnessite layer is an oxygen sheet in which O_{layer} occupy A sites, that Mn cations fill octahedral b positions, and that the upper surface is formed by O_{layer} in C sites. Such a layer can be symbolically represented as AbC. In the simulation of idealized polytypes, it is assumed that the O_{layer} in the lower sheet of the next birnessite layer in a stack can occupy A, B or C positions. If these O_{layer} are located in C sites, O_{layer} from adjacent layers define interlayer prisms. This type of interlayer will be referred to as a P-type interlayer and denoted with an equal sign (=). If they are located in A or B sites, O_{layer} from adjacent layers define interlayer octahedra. These interlayers are referred to as O-type and denoted with a dash sign (–) to distinguish them from the P-type interlayers. Using the above notions, a one-layer polytype having O-type interlayer (Fig. 1a) can be represented as:

AbC – AbC… 1*H*

Systematic consideration of possible two-layer polytypes leads to two independent hexagonal polytypes having homogeneous interlayers (Figs. 1b-c):

147 AbC = CbA = AbC… $2H_1$

148 AbC – AcB – AbC… $2H_2$

149 With this notation the first digit indicates the number of layers per unit-cell, the letter
150 corresponds to the layer symmetry (*H*, *R*, and *M* standing for hexagonal, rhombohedral, and
151 monoclinic, respectively), and the final numerical subscript determines the polytype. In $2H_1$
152 and $2H_2$ polytypes adjacent layers are rotated with respect to each other by 180° around the
153 axis parallel to the **c** axis and passing either through Mn atoms of adjacent layers ($2H_1$) or
154 through the "lower" O_{layer} (A sites – $2H_2$). In 1*H* and $2H_1$ the Mn_{layer} octahedral sites overlap
155 in projection on the **ab** plane, whereas these sites are distributed more homogeneously in $2H_2$.

156 Analysis of three-layer polytypes leads to two independent modifications with
157 rhombohedral symmetry (3*R*). These two polytypes differ from each other by their interlayer
158 structures (Figs. 2a-b):

159 AbC = CaB = BcA = AbC … $3R_1$

160 AbC – BcA – CaB – AbC … $3R_2$

161 Two additional three-layer polytypes having O-type interlayers and hexagonal
162 symmetry may also be derived (Figs. 2c-d):

163 AbC – AcB – AcB – AbC … $3H_1$

164 AbC – AcB – CaB – AbC … $3H_2$

165 In terms of the C-centered orthogonal unit cell successive layers in $3R_1$ and $3R_2$
166 polytypes are shifted by -*a*/3 and +*a*/3, respectively. As in $2H_2$ polytype successive layers in
167 $3H_1$ and $3H_2$ polytypes are not related by the same interlayer displacement. In addition, layers
168 from different layer pairs are related to each other by different elements of symmetry in $3H_1$
169 and $3H_2$ polytypes. For example, layers in the first layer pair of the $3H_1$ polytype are related
170 by a 180° rotation along the **c** axis passing through A sites, whereas they are superimposed in
171 the second pair (Fig. 2c). In the latter layer pairs, Mn octahedral sites overlap in projection on

the **ab** plane, whereas in $3R_1$, $3R_2$ and $3H_2$ polytypes, layer Mn cations are distributed homogeneously among all possible sites (Figs. 2a, b, d).

Heterogeneity arising from the coexistence of O- and P-type interlayers in a given birnessite polytype is likely not energetically favorable. Polytypes with alternating O- and P-type interlayers were thus excluded from the current study. However, transformation from one polytype to the other likely often occurs through layer translations. Such displacements occur, for example, as a result of cation exchange or during hydration-dehydration processes. Therefore, among birnessite polytypes some unusual modifications can be formed from one-layer polytype by shifting the layers. For example, a two-layer structure AbC – BcA = AbC with both interlayer types can be obtained if successive layers are shifted alternately by +a/3 and -a/3 along the **a** axis of the C-centered unit cell.

The above idealized birnessite polytypes are similar to those of oxides with general formula A_xMO_2 (Delmas et al. 1980). These authors deduced four polytypes, T1, P2, P3, and O3, which correspond to $1H_1$, $2H_2$, $3R_1$, and $3R_2$ modifications in the present nomenclature. Birnessite polytypes are also similar to those of natural and synthetic layer double hydroxides $(R^{2+}_{1-x}R^{3+}_{x})(OH)_2(CO_3,SO_4)_{x/2}$ (Drits 1987; Bookin and Drits 1993) and to those of other natural and synthetic layered compounds (Bailey 1980).

Layer symmetry and polytype diversity

Structural characterization of birnessite shows layers with either hexagonal or pseudo-hexagonal symmetry. Birnessite has an hexagonal layer symmetry when octahedral vacancies represent the major source of layer charge deficit (Giovanoli et al. 1970b; Chukhrov et al. 1985; Silvester et al. 1997; Lanson et al. 2000; 2002b; Gaillot et al. 2003; 2005). By contrast, birnessite has an orthogonal layer symmetry when the main source of negative charge in vacancy-free layers is the presence of a high amount of Mn^{3+} cations (Post and Veblen 1990;

Drits et al. 1998; Lanson et al. 2002a; Gaillot et al. 2004). In the latter case the layers have a C-centered unit-cell with $a > b\sqrt{3}$ (Burns and Burns 1977; Chukhrov et al. 1985; Post and Veblen 1990; Gorshkov et al. 1992; Drits et al. 1997a, 1998; Lanson et al. 2000, 2002a, 2002b; Gaillot et al. 2003, 2004, 2005). Orthogonal layer symmetry results from the distortion of Mn^{3+}-octahedra because of the Jahn-Teller effect (Drits et al. 1997a). In Mn^{3+} octahedra, two Mn^{3+}-O distances are indeed much longer than the other four. For example, in crednerite $CuMnO_2$ Mn^{3+}-octahedra contain two 2.26 Å and four 1.929Å bond lengths with an average <Mn-O> distance of 2.04 Å (Töpfer et al. 1995). Similar distortions of Mn^{3+}-octahedra have been reported by Shannon et al. (1975) for α-MnOOH (2.041 Å – Glasser and Ingram 1968), γ-MnOOH (2.037 Å – Dachs 1963) and α-Mn_2O_3 (2.039-2.045 Å – Norrestam 1967). The random distribution of Mn^{4+} and Mn^{3+} cations combined with a random azimutal orientation of the long Mn^{3+}-O bonds of the Mn^{3+} octahedra would lead to unfavorable steric strains, because of the distortion of Mn^{3+}-octahedra. An ordered distribution of Mn^{3+}-octahedra all having the same azimutal orientation allows minimizing these strains. According to SAED results, in vacancy-free birnessite layers Mn^{3+} are distributed in rows parallel to the **b** axis and have their long Mn^{3+}-O bonds parallel to the **a** axis (Drits et al. 1997a, 1998; Lanson et al. 2002a; Gaillot et al. 2004). Because of the systematic elongation of Mn^{3+}-ocathedra along the **a** axis and because the four short Mn^{3+}-O distances (1.92-1.93 Å) are similar to Mn^{4+}-O bond lengths (1.912 Å for λ-MnO_2), *b* parameters are similar (2.83-2.85 Å) in most natural and synthetic birnessite samples regardless of the average valency of the Mn_{layer} (Chukhrov et al. 1985; Post and Veblen 1990; Chen et al. 1996b; Ching et al. 1997a; Drits et al. 1997a, 1998; Kim et al. 1999; Lanson et al. 2000, 2002a, 2002b; Gaillot et al. 2003, 2004, 2005).

The transition from birnessite having layers with hexagonal symmetry to that having pseudo-hexagonal symmetry leads to a modification of symbol notation for the corresponding polytypes. Specifically, hexagonal one-, two-, and three-layer polytypes (1*H*, $2H_1$, $2H_2$, $3H_1$

222 and $3H_2$) are changed to the corresponding orthogonal ones ($1O$, $2O_1$, $2O_2$, $3O_1$ and $3O_2$)
223 whereas $3R_1$ and $3R_2$ are changed to $1M_1$ and $1M_2$ monoclinic modifications having $-a/3$ and
224 $+a/3$ displacements of adjacent layers along the **a** axis (Table 1). In $1M_1$ and $1M_2$ birnessite
225 adjacent layers may be shifted along the **a** axis by values different from $\pm 0.333a$ (Post and
226 Veblen 1990; Lanson et al. 2002b).
227
228 **Cation composition, interlayer structure, and polytype diversity**
229 The arrangement of adjacent layers in different polytypes, the presence or absence of
230 vacant layer octahedral sites, the nature of interlayer cations, and their local environments are
231 interrelated structural characteristics. Therefore, it is reasonable to define possible interlayer
232 structures for each particular layer stacking and specifically to propose optimum positions for
233 interlayer cations as a function of their ionic radius and valency (Table 2). This approach also
234 relies on existing birnessite structure models (Chukhrov et al. 1978, 1985; Post and Veblen
235 1990; Drits et al. 1997a, 1998, 2002; Kim et al. 1999; Lanson et al. 2000, 2002a, 2002b;
236 Manceau et al. 2002; Gaillot et al. 2003, 2005). To symbolize positions for interlayer water
237 molecules ($H_2O_{interlayer}$) and cations the capital letters A', B', and C', and corresponding lower
238 case a', b', and c' will be used, respectively.
239 **Polytypes with hexagonal layer symmetry**. The presence of layer vacancies allows
240 interlayer cations to share one face with vacant octahedra so as to provide local charge
241 compensation to undersaturated O_{layer}. If birnessite interlayers contain relatively small di- or
242 tri-valent cations, such as $Mn^{2+,3+}$, $Co^{2+,3+}$, Cu^{2+}, Ca^{2+}, and Mg^{2+}, then they are commonly
243 octahedrally coordinated by O_{layer} bound to layer vacancies and $H_2O_{interlayer}$. Depending on the
244 layer stacking mode the presence of octahedrally coordinated interlayer cations located above
245 and/or below layer vacancies can give rise to three types of bonding between $H_2O_{interlayer}$ and
246 the nearest O_{layer} from the adjacent layer. In the first [model 1a (polytype $1H$)] strong H-bonds

247 link these species as they form empty prisms with short $H_2O_{interlayer}$-O_{layer} distances along the
248 prism edges (2.70-2.75 Å – Fig. 3a). In the second [model 2a (polytype $3R_1$), model 3a
249 (polytype $3R_2$), and model 4a (polytype $2H_1$)] O_{layer} and $H_2O_{interlayer}$ are linked by weak H-
250 bonds as they form empty octahedra with long $H_2O_{interlayer}$-O_{layer} distances (3.0-3.15 Å – Fig.
251 3b). In the third interlayer type [model 5a (polytype $2H_2$), model 6a [polytype $3H_1$], and
252 model 7a (polytype $3H_2$)] empty prisms and empty octahedra formed by O_{layer} and $H_2O_{interlayer}$
253 coexist within a given interlayer, with prisms located on one side of the interlayer and
254 octahedra on the opposite one (Fig. 3c).

255 The presence of tetrahedrally coordinated interlayer cations located above and/or
256 below the vacant layer octahedra in model 3b (polytype $3R_2$) is associated with the formation
257 of strong H-bonds between $H_2O_{interlayer}$ coordinating the interlayer cations and nearest O_{layer}
258 from the adjacent layer. Both species are superimposed in projection on the **ab** plane and thus
259 located close to each other (Fig. 3d). The coexistence of both octahedrally and tetrahedrally
260 coordinated interlayer cations in model 5c (polytype $2H_2$) leads to the formation of empty
261 prisms between the $H_2O_{interlayer}$ and O_{layer} (strong H-bonds) on one side of the interlayer and to
262 short $H_2O_{interlayer}$-O_{layer} distances on the other side (not shown).

263 On the other hand, if birnessite interlayers contain large mono- or di-valent cations,
264 such as K^+, Ba^{2+}, Sr^{2+}, Cs^+, then they will be located in the interlayer mid-plane either in
265 octahedra defined by O_{layer} from adjacent layers [model 5b (polytype $2H_2$), and model 6b
266 (polytype $3H_1$)] or in interlayer prisms [model 2b (polytype $3R_1$)]. In the latter case, interlayer
267 prisms share one face with a layer octahedron and three edges with occupied octahedra of the
268 adjacent layer. Local charge compensation is achieved when interlayer cations are distributed
269 so that prisms share a face with vacant layer octahedra. Random distribution of interlayer
270 cations leads to electrostatic repulsion with Mn_{layer} despite the presence of layer vacancies.
271 Table 2 lists birnessite polytypes consisting of hexagonal vacancy-bearing layers that differ

from each other by stacking modes and interlayer structures, which are reasonable from a crystal chemical point of view.

Polytypes with orthogonal layer symmetry. The interlayer cations for vacancy-free layers should have six-fold coordination by O_{layer} and $H_2O_{interlayer}$, and distributed so as to avoid direct interaction with Mn_{layer}. The 1*O*, 2O_2, 3O_1, and 3O_2 polytypes are thus not suitable to host large mono- or divalent cations as they cannot avoid such interactions. In contrast, the 1M_2 and 2O_1 polytypes can host these cations in the interlayer mid-plane, with octahedral [model 3e (polytype 1M_2)], or prismatic [model 4c (polytype 2O_1), and model 4e (polytype 2O_1)] coordinations.

Model 2c (polytype 1M_1) represents a special case as interlayer cations cannot be located in a' or b' sites because of the interaction with Mn_{layer}. However, smaller interlayer cations, such as Na^+, can be located, together with $H_2O_{interlayer}$, in the interlayer mid-plane above and/or below O_{layer} of adjacent layers as was described for Na-rich synthetic birnessite, hereafter referred to as NaBi (Lanson et al. 2002b). Similarly, in Na^+-saturated 2O_1 polytype the interlayer cations are likely located above and/or below O_{layer} from adjacent layers (model 4e).

Relatively small di- and tri-valent interlayer cations may be located above and/or below empty layer tetrahedra (tridentate cavities) sharing three edges with layer Mn octahedra (^{VI}TE sites). The $H_2O_{interlayer}$ provides octahedral coordination to these cations and may form either empty prisms [model 3d (polytype 1M_2) – Fig. 4a] or empty octahedra [model 1b, (polytype 1*O*), and model 4d (polytype 2O_1) – Fig. 4b], with O_{layer} from the adjacent layer. Empty prisms and empty octahedra coexist within a given interlayer [model 5d (polytype 2O_2)] if interlayer cations are octahedrally coordinated. If interlayer cations have both octahedral and tetrahedral coordination then $H_2O_{interlayer}$ and O_{layer} in model 5e (polytype 2O_2) form empty prisms and strong H-bonds on either side of a given interlayer.

297 Vacancy-free birnessite layers can have hexagonal symmetry if the long Mn^{3+}-O
298 bonds of the layer Mn^{3+}-octahedra are randomly oriented with respect to the **a** axis by n60°
299 (Gaillot et al. 2005, 2006a). Interlayer cations in such birnessite layers should be distributed
300 so as to avoid direct interaction with the nearest Mn_{layer}. In this case, suitable interlayer
301 structures are those described for vacancy-free orthogonal layers (Table 2).
302
303 ## CALCULATION OF XRD PATTERNS
304
305 The XRD patterns calculated for polytypes with the same layer symmetry and
306 periodicity along the **c*** axis have the same d-spacings, but differ by their *hkℓ* intensity
307 distributions. Characterization of layer silicates has shown that structures can be
308 approximated by models for polytype identification purpose. The influence of the actual layer
309 structure on the *hkℓ* intensity distributions is indeed a second-order effect compared to the
310 differences between polytypes (Bailey 1980). Structure models were thus proposed for each
311 birnessite variety and corresponding powder XRD patterns were calculated. All calculations
312 were performed using the program developed by Plançon (2002) on the basis of the formalism
313 described by Drits and Tchoubar (1990). No orientation function was considered, and no
314 random stacking faults were introduced for the calculations.
315
316 ### Initial structure models
317 In all structure models, Mn_{layer} and O_{layer} occupy special sites in the orthogonal C-
318 centered unit-cell: (0, 0, 0), (0.333, 0, z) and (-0.333, 0, -z), respectively, where z-coordinates
319 (in projection on the **c*** axis) were equal to 1.00Å (Post and Veblen 1990; Drits et al. 1998;
320 Lanson et al. 2000, 2002a, 2002b; Gaillot et al. 2003, 2005). According to the close-packing
321 notation interlayer cations and $H_2O_{interlayer}$ also occupy special sites. In the initial structure

322 models, the z-coordinates of the interlayer cations (Me) and $H_2O_{interlayer}$ are the sole variable
323 parameters. The initial z-coordinates of Me and H_2O molecules can be estimated from typical
324 Me-O and Me-H_2O bond lengths for four- and six-fold coordinated Me and from elementary
325 geometrical relationships between these bond lengths and corresponding z-coordinates. For
326 example, if an interlayer cation is octahedrally coordinated above and/or below a vacant layer
327 octahedron, then the following equations are deduced from the hexagonal symmetry of the
328 layer (Lanson et al. 2002b):

329 $$z(Me) = z(O_{layer}) + \sqrt{d^2(Me-O) - b^2/3} = z(O_{layer}) + \Delta z$$

330 and $$z(H_2O) = z(O_{layer}) + 2\Delta z$$

331 In the present work, Me-O and Me-H_2O interatomic distances were determined from
332 the effective ionic radii given by Shannon (1976). Where applicable the interlayer atomic
333 positions were adapted from published structural determination of synthetic Na-birnessite
334 (Lanson et al. 2002a), Ca-birnessite (Drits et al. 1998), H-birnessite (Lanson et al. 2000), and
335 K-birnessites (Gaillot et al. 2003, 2005). In the various structure models K, Ca, Mn, Na,
336 and/or Mg were used as interlayer cations. For the different structure models presented in
337 Table 2, corresponding atomic positions and their occupancies are listed in Table 3.
338
339 **Calculated XRD patterns**
340 Powder XRD patterns calculated for the different polytypes are shown in Figures 5-8,
341 whereas d-values and *hkℓ* indices of reflections observed on the various patterns are listed in
342 Table 4. Indexing is performed assuming an orthogonal C-centered cell for both hexagonal
343 and orthogonal birnessite. Reflections in the 36-64° 2θ CuKα range have 20ℓ,11ℓ indices (10ℓ
344 and 01ℓ when using a hexagonal unit-cell), whereas they have 31ℓ,02ℓ indices (11ℓ when
345 using a hexagonal unit-cell) over the 64-75° 2θ CuKα range. The XRD patterns shown in

346 Figure 5 correspond to structure models in which interlayer Mn cations are located above
347 and/or below layer sites and are octahedrally coordinated by O_{layer} and $H_2O_{interlayer}$ (^{VI}TC sites
348 – Table 3). The calculated XRD patterns (Figure 5) can be used to identify vacancy-bearing
349 birnessite having one-, two- and three-layer periodicity along the **c** axis and different layer
350 stacking. However, analysis of the XRD patterns calculated for a given birnessite polytype
351 having different interlayer structures shows that for a given birnessite polytype the intensity
352 of $hk\ell$ reflections also depends on the chemical nature of interlayer cations, their distribution
353 and local environment. For example, interlayer spaces of $3R_2$ polytype (models 4a and 4b)
354 may be occupied by Zn cations having octahedral and/or tetrahedral coordination (Manceau et
355 al. 2000c; Lanson et al. 2000, 2002a) and located in TC sites or TE sites. The replacement of
356 tetrahedrally for octahedrally coordinated Zn cations leads to a significant decrease of
357 204/114, 208/118 and 20.10/11.10 peak intensity (104, 018 and 10.10 assuming a hexagonal
358 cell), with respect to the strongest $20\ell/11\ell$ reflections (Figs. 6a-b). Location of Zn cations in
359 ^{IV}TE sites [model 3c (polytype $3R_2$) – Fig. 6c] strongly increases the 204/114 and 207/117
360 reflection intensities, with respect to 201/111. Important redistribution of intensities is
361 observed also for the $2O_1$ and $1M_2$ polytypes when interlayers are occupied either by large K^+
362 (models 4c and 3e) or by smaller Ca^{2+} (models 4d and 3d). The transition from model 3e to
363 model 3d significantly increases 201, 110, 112, 203 and 11-2 and decreases the 111 and 113
364 intensities (Figs. 7a-b). Similarly, the transition from model 4c to 4d is accompanied by
365 redistribution of the 112 and 114 maxima: strong 112 and moderate 114 peaks for model 4c
366 are replaced by strong 114 and moderate 112 ones for model 4d (Figs. 7c-d).

367 In contrast, the relative intensity of strong, moderate and weak reflections change very
368 little for the $3R_1$ polytype when interlayers are occupied by either K^+, Ca^{2+}, or Mn^{3+}. The only
369 significant change in the MnBi XRD pattern compared to KBi is a strong increase of 201/111
370 intensity (Figs. 8a-b). For the $2H_1$ polytype, a strong increase of 200 and 203 intensities and a

limited increase of the 206 one is visible on the XRD pattern calculated for MnBi model compared to KBi (models 4and 4b – Figs. 8c-d)

The calculated XRD patterns show the limited influence of the interlayer structure on the *hkℓ* intensity distribution for a given birnessite polytype. The intensity distribution is primarily determined by the polytype (Figs. 6-8). As a consequence, identification of birnessite polytypes having either hexagonal or C-centered orthogonal ($a > b\sqrt{3}$) unit cells may be performed without *a priori* details of their layer and interlayer structures.

DISCUSSION

Criteria for determination of birnessite polytypes

Birnessite polytypes having the same periodicity along the **c** axis, but with different layer symmetry, differ from each other by the number of *hkℓ* reflections. For example, the hexagonal birnessite exhibits a single series of $20\ell/11\ell$ reflections, whereas 20ℓ and 11ℓ series of reflections are individualized for birnessite with an orthogonal layer symmetry. In addition, XRD patterns of hexagonal birnessite usually contains a diagnostic 310/020 reflection (110 when using the hexagonal cell) with $d = (1.42 \pm 0.01)$ Å whereas for the orthogonal birnessite this reflection is split with $d(310) > d(020) = (1.42 \pm 0.01)$ Å.

Birnessites with similar periodicity and layer symmetry can be differentiated by the intensity distribution of *hkℓ* reflections. Figures 9a-b show that *hkℓ* reflections with $\ell = 2n$ are more intense for $2H_1$ polytype compared to those of $2H_2$ polytype. In contrast, $20\ell/11\ell$ reflections (10ℓ and 01ℓ when using the hexagonal cell) with $\ell = 2n + 1$ are significantly stronger for $2H_2$ polytype. Similarly, 11ℓ and 20ℓ reflections with $\ell = 2n$ are stronger than those with $\ell = 2n + 1$ for the $2O_1$ polytype (Fig. 9c). XRD patterns from $3R_1$ and $3R_2$ polytypes

also differ from each other by their intensity distributions among $hk\ell$ reflections. The $20\ell/11\ell$ reflections with $\ell = 3n - 1$ (01ℓ with $\ell = 3n - 1$ ones if using the hexagonal cell) are intense for $3R_1$ polytype but not for $3R_2$, whereas $20\ell/11\ell$ reflections with $\ell = 3n + 1$ (10ℓ with $\ell = 3n + 1$ ones if using the hexagonal cell) are intense for $3R_2$ polytype and weak for $3R_1$ (Figs. 10a-b). $3H_1$ and $3H_2$ polytypes differ from $3R_1$ and $3R_2$ by the presence of $20\ell/11\ell$ reflections with $\ell = 3n$ (Figs 10c-d). Similarly, intensity of $20\ell/11\ell$ reflections with $\ell = 3n$ (10ℓ with $\ell = 3n$ if using the hexagonal cell) is significantly lower for $3H_2$ than for $3H_1$ (Figs. 10c-d). The intensity distribution among $hk\ell$ reflections described above for $3R_1$, $3R_2$, $3H_1$ and $3H_2$ polytypes remain valid for the equivalent birnessite polytypes with orthogonal layer symmetry ($1M_1$, $1M_2$, $3O_1$, $3O_2$).

Special attention should be paid to identify one- ($1H$ and $1O$) and two-layer ($2H_1$ and $2O_1$) polytypes having the same layer symmetry. The presence of a weak 203/113 reflection is the sole distinguishing feature allowing identification of the two-layer polytypes (Figs. 5a-b). Note that the difference between XRD patterns corresponding to these two polytypes is further reduced when $1H$ layer pairs are present in the $2H_1$ polytype (that is when AbC – AbC pairs are present in crystals dominated by AbC = CbA = AbC… sequences) as the intensity of the 203/113 reflection is significantly decreased by the presence of such $1H$ layer pairs in a mixed-layered structure (not shown).

Stacking faults

The above described method can be used not only for the identification of birnessite polytypes and also to determine the nature of stacking faults which are typically present in natural and synthetic birnessites. Well-defined and random stacking faults significantly alter XRD patterns from defective layer structures (for definition of well-defined and random

419 stacking faults see Drits and Tchoubar, 1990). Well-defined stacking faults correspond to the
420 interstratification of layer pairs having the same thickness but different internal structure and
421 interlayer displacements within a periodic polytype. As the result of such interstratification,
422 *hkℓ* reflections are shifted, and their positions become irrational.

423 Drits and McCarty (1996) have shown that Méring's rules, initially proposed for basal
424 reflections (Méring 1949), can be generalized to account for the behavior of *hkℓ* reflections
425 from defective layer structures. According to these generalized rules, *hkℓ* reflections observed
426 from a defective layer structure are located between neighboring *hkℓ* reflections of periodic
427 phases whose fragments (layer pairs in the present case) are interstratified. The actual position
428 of *hkℓ* reflections corresponding to the defective layer structure depends on the relative
429 proportion of the structure fragments and on relative intensities of the "involved" *hkℓ*
430 reflections of the periodic phases.

431 For example, Lanson et al. (2002b – Fig. 3) showed that reflections of Zn-sorbed
432 birnessite are located between *hkℓ* reflections calculated for $3R_2$ and 1*H* polytypes and
433 hypothesized that the main $3R_2$ polytype contained some 1*H* layer pairs (i.e. AbC – AbC pairs
434 are present in crystals dominated by AbC – BcA – CaB – AbC … sequences). As a result,
435 positions of *hkℓ* reflections of the main $3R_2$ polytype should indeed be shifted from their ideal
436 position towards those of the defect-free 1*H* polytype. Accordingly, the best agreement
437 between experimental and calculated XRD patterns was obtained for a defective $3R_2$ polytype
438 containing 12% of 1*H* layer pairs (Lanson et al. 2002b). A similar approach may be applied to
439 mixtures containing periodic and defective birnessites. For example, Figure 11 shows the best
440 possible agreement between an experimental XRD pattern and that calculated for a mixture of
441 four birnessites: a periodic $2H_1$ polytype and three defective ones ($2O_1/2H_1$, $2H_1/3R_1$, and
442 $3R_1/2H_1$). In the three mixed-layered structures, layer pairs of the $2H_1$ polytype are randomly

443 interstratified with those of the $2O_1$ and $3R_1$ polytypes in proportions 1:1, 7:3, and 1:9,
444 respectively. Note on Figure 11 that each of these mixed-layered structures gives a diagnostic
445 contribution to the calculated XRD pattern (Gaillot et al. 2004).

446 In our experience, one of the most effective way to study defective birnessite is to
447 combine the above rules for polytype identification and interstratification to build up starting
448 models for XRD pattern calculation (Manceau et al. 1997; Drits et al. 1998; Lanson et al.
449 2000, 2002a, 2002b; Gaillot et al. 2003, 2004, 2005). Defective birnessite may contain layer
450 pairs which were not reported so far for natural and synthetic periodic birnessite. Therefore,
451 all theoretically possible birnessite polytypes should be considered to determine the nature of
452 stacking faults XRD by comparing experimental and calculated XRD patterns.

453

454 **Birnessite polytypes reported for natural and synthetic birnessites**

455 **1*H* Polytype**. The first detailed structural study of natural birnessite was performed by
456 Chuckhrov et al. (1985) on monomineralic birnessite micronodules dredged from the oceanic
457 floor. The sample has a one-layer hexagonal unit-cell and its structure corresponds to the 1*H*
458 ploytype (model 1a) in which interlayer Mn^{3+} and Mg^{2+} cations are octahedrally coordinated
459 above and/or below vacant layer octahedra. Ca^{2+} and Na^{+} cations were also present in the
460 interlayer. This structure model was further supported by X-ray absorption spectroscopy data
461 (Manceau et al. 1992a, 1992b). Analysis of published experimental XRD patterns shows that
462 1*H* birnessite dominates in Mn-nodules from ocean and lake floors (Burns and Burns 1977;
463 Drits et al. 1985). This 1*H* polytype occurs also in soil birnessite (Glover 1977).

464 Birnessite resulting from the equilibration at low pH of NaBi (obtained according to
465 the Giovanoli protocol – Giovanoli et al. 1970b) was studied by Silvester et al. (1997), Drits
466 et al. (1997a) and in more details by Lanson et al. (2000). This proton-rich birnessite,
467 hereafter referred to as HBi, has a one-layer hexagonal unit cell and a structure similar to

model 1a. HBi can thus be considered a synthetic analogue of natural 1*H* birnessite. As natural 1*H* birnessite, HBi layers contain a significant amount of vacant layer octahedra capped by Mn^{2+} and Mn^{3+}. The negative layer charge of HBi is compensated for by protons and interlayer Mn cations, and the distribution of layer vacancies is inherited from the ordered Mn^{3+} distribution in NaBi. The $H_2O_{interlayer}$ provides octahedral coordination to $Mn_{interlayer}$ and forms empty prisms, and strong H-bonds, with O_{layer} of the adjacent layer. Manceau et al. (1997) and Lanson et al. (2002b) showed that equilibration of NaBi in the presence of aqueous heavy metals (Co, Cd and Pb) leads also to the formation of the 1*H* polytype (model 1a). When Zn^{2+} is present, the resulting Zn-sorbed synthetic birnessite (ZnBi) has a $3R_2$ polytype, in which models 3a and 3b coexist. Interlayer Zn^{2+} cations are systematically located above and/or below vacant layer sites but can have both octahedral and tetrahedral coordinations. As a result, $H_2O_{interlayer}$ providing octahedral (model 3a) and tetrahedral (model 3b) coordination of Zn form weak and strong H-bonds, respectively, with O_{layer} of the adjacent layer.

1M_1 Polytype. Na-rich birnessite synthesized at high pH (Giovanoli et al. 1970a) was first described by Post and Veblen (1990) as a one-layer monoclinic polytype (1M_1 polytype, model 2c). To refine the structure they used *C*2/*m* space group and the Rietveld technique. However, their results were not precise enough to draw definitive conclusions on the origin of the layer charge. Lanson et al. (2002a) showed that NaBi has a one-layer triclinic unit-cell ($C\bar{1}$ space group) and consists of vacancy-free layers, the layer negative charge arising from the Mn^{3+}-for-Mn^{4+} substitution within octahedral layers. The orthogonal layer symmetry results from the Jahn-Teller distortion of Mn^{3+}-octahedra which all have their long Mn^{3+}-O_{layer} bond oriented along the **a** axis. Structural sites of interlayer Na and H_2O, and their occupancies, have also been determined. The triclinic character of NaBi originates from a small layer displacement along the **b** axis.

493 NaBi varieties with different monovalent and divalent cations that were exchanged for
494 Na^+ were studied by Post and Veblen (1990), Kuma et al. (1994) and Bartoli (1997). XRD
495 patterns of these different birnessites can be indexed with a one-layer monoclinic unit-cell
496 whose parameters depend on the interlayer cation. However, essential details of these
497 birnessites remain poorly understood. For example, Mg^{2+} cations in Mg-exchanged birnessite
498 (MgBi) are supposedly located almost above or below octahedral sites (Post and Veblen
499 1990). Such a location is possible for interlayer Mg^{2+} cations only if the underlying octahedral
500 sites are vacant, NaBi layers being vacancy-free.

501 Similarly, Bartoli (1997) reported in K-exchanged birnessite the location of K^+ cations
502 in either a' or b' sites, whereas the presence of K^+ cations in these sites would lead to their
503 direct interaction with Mn_{layer} from adjacent layers, as can be seen from symbolic notations
504 (Model 2c – Table 2). Post and Veblen (1990) reported K^+ positions in KBi that are shifted
505 from the center of the interlayer prism toward its edges.

506 Ca^{2+}-for-Na^+ exchange in NaBi dramatically modifies the initial one-layer triclinic
507 structure of NaBi (model 2c) leading to a four-layer polytype in which layer pairs having
508 orthogonal stacking are shifted alternately by $\pm b/2$ along the **b** axis (Drits et al. 1998).
509 Gorshkov et al. (1992) described an occurrence of natural Ca-bearing birnessite, which was
510 analogous to the synthetic Ca-exchanged variety of NaBi.

511 **$3R_1$ Polytype**. Chen et al. (1996b) synthesized K-rich birnessite (KBi) with a $3R_1$ unit-
512 cell (model 2b). The KBi layers contain only Mn^{4+} and vacancies. From the refinement of
513 integrated intensities they concluded that both K^+ and $H_2O_{interlayer}$ were not located in the
514 prism's centers (a' and b' sites) as in the idealized model 2b but rather in the center of the
515 prism's faces. Gaillot et al. (2005) further refined this structure and showed that interlayer
516 prisms contain three possible K sites, each shifted from the faces of the prism toward its
517 center. Similar positions of interlayer cations were found for Cs^+, Ba^{2+} and Sr^{2+}-exchanged

518 KBi (Gaillot et al. 2006b). The Ca^{2+}-for-K^{+} exchange in KBi modifies the initial layer
519 stacking from the $3R_1$ polytype (model 2b) to the 1*H* one (model 1a). The driving force for the
520 KBi-to-CaBi transformation is likely the possibility of forming strong H-bonds between
521 $H_2O_{interlayer}$ providing octahedral coordination of Ca cations and O_{layer} of the adjacent layer
522 (model 1a). Using mild hydrothermal conditions, Chen et al. (1996a) and Gaillot et al. (2005)
523 synthesized directly Na-rich birnessite ($NaBi_h$) having a $3R_1$ unit-cell. According to these
524 authors, these $NaBi_h$ layers consist of Mn^{4+} cations and vacant octahedra but positions of
525 interlayer Na^{+} were not determined.

526 **$2H_1$ Polytype**. Kim et al. (1999) synthesized K-rich birnessite (KBi) from the
527 decomposition of $KMnO_4$ at temperatures ranging from 200-1000°C. Using the Rietveld
528 technique, these authors showed that KBi obtained at 800°C has two-layer hexagonal
529 symmetry because of the regular alternation of octahedral layers rotated with respect to each
530 other by 180° around the axis passing through layer Mn cations (polytype $2H_1$, model 4b).
531 Gaillot et al. (2003) has shown that the actual structure of KBi obtained at 800°C differs from
532 the model of Kim et al. (1999) by several important details. First, KBi interlayers have
533 heterogeneous cation composition with the coexistence of both K^{+} and Mn^{3+} cations; second,
534 because of the layer-to-interlayer migration of Mn^{3+} cations KBi layers contain only Mn^{4+}
535 cations and vacant octahedra. Finally, interlayer K^{+} is not located in the prism's center. Rather
536 K^{+} is distributed over three possible sites, each of which being shifted from the center of the
537 prism towards it faces. Thus, the idealized KBi structure corresponds to the coexistence of
538 models 4a and 4b ($2H_1$ polytype).

539 **$2O_1$ Polytype**. KBi synthesized from the thermal decomposition of $KMnO_4$ at 1000°C
540 has vacancy-free layers and orthogonal layer symmetry (polytype 2O1, model 5c – Gaillot et
541 al. 2005, 2006a).

542 **Ambiguously determined polytypes**. Kim et al. (2000) used the Rietveld technique
543 to determine structures of synthetic K-Li-rich birnessites (Li-K-Bi) obtained from the thermal
544 decomposition of a Mn-KNO_3-LiOH mixture at 800°C and 1050°C. They concluded that the
545 800°C Li-K-Bi has a three layer periodicity and hexagonal symmetry of layers whereas the
546 1050°C Li-K-Bi has an orthogonal layer symmetry and two-layer periodicity due to an
547 ordered rotation of layers by 180°. However, the description of these structures was rather
548 confusing because of technical errors. In particular, symbolic notations for the structures do
549 not correspond to the proposed structure models. For example, the 1050°C Li-K-Bi is
550 described as AaB a' BbA b' instead of the actual notation given for model 4b (AcB a' BcA).
551 In addition, unit-cell parameters given for the 1000°C Li-K-Bi are not consistent with the
552 proposed space group. Similarly, interatomic Mn-O distances differ significantly from those
553 expected when heterovalent Mn_{layer} cations coexist within the octahedral layers. These authors
554 also describe the structure of the Li-K-Bi sample synthesized at 800°C as AcB a' CbA c' BaC
555 b' (model 3d, polytype $3R_2$), with octahedrally coordinated interlayer K^+ cations. However,
556 atomic coordinates reported for this sample (Table 1 – Kim et al. 2000) correspond to
557 polytype $3R_1$ (model 2b) with interlayer K^+ having prismatic coordination. This latter
558 structure model is consistent with the experimental XRD pattern reported for this sample
559 (Figure 4 – Kim et al. 2000) which is similar to those obtained by Chen et al. (1996a) and
560 Gaillot et al. (2005) from $3R_1$ polytypes (model 2b) synthesized under mild hydrothermal
561 conditions. All these experimental patterns are similar to the one displayed on Figure 8a.

562 **Turbostratic samples**. Finally, one has to note that among different natural
563 environments, and especially in soils, turbostratic birnessite is extremely common. For
564 example, turbostratic birnessite has been reported as resulting from the bacterial oxidation of
565 Mn^{2+} by different strains (Mandernack et al. 1995; Villalobos et al. 2003; Jurgensen et al.
566 2004; Bargar et al. 2005; Webb et al. 2005) and from abiotic processes (Mandernack et al.

567 1995). However, so far there is little unambiguous information derived from XRD data on the
568 structural and crystal chemical of these varieties. Most often the structural characterization of
569 disordered birnessite is limited to the description of 00*l* peak positions as a function of
570 relative humidity to assess the lamellar character of these "poorly crystalline birnessites". The
571 position of *hkl* reflections has also been used to hypothesize the actual layer symmetry (and
572 thus the origin of the layer charge of these varieties) however without much experimental
573 support (Villalobos et al. 2003; Jurgensen et al. 2004; Webb et al. 2005).

574 However, as described, birnessite having different layer symmetry may be
575 unambiguously distinguished from each other from the shape of their *hk* bands (Fig. 12). A
576 shoulder, resulting from the individualization of 20 and 11 reflections, is indeed visible on the
577 low-angle side of main maximum of the 20,11 band for orthogonal modifications (at ~2.55 Å
578 and 2.45 Å, respectively – Fig. 12b), whereas this shoulder is logically absent for hexagonal
579 modifications (Fig. 12a). Similarly, the 31,02 band of the orthogonal modifications contains
580 two distinct maxima (~1.474 Å and 1.422 Å – Fig. 12b) which are merged for the hexagonal
581 modifications (peak at ~1.422 Å – Fig. 12a). The features described for the orthogonal
582 modifications are like those reported for the Mn oxides resulting from the oxidation of Mn^{2+}
583 by *Bacillus sp*. strain SG-1 (Fig. 3 in Webb et al. 2005) indicating the presence of a high
584 proportion of Mn^{3+} within the octahedral layers of this birnessite. The presence of Mn^{3+}-rich
585 rows in vacancy-free layers, as in NaBi, is also supported by the splitting of the 8 $Å^{-1}$ feature
586 in the EXAFS spectra (Fig. 5 in Webb et al. 2005) which has been described as characteristic
587 of the presence of Mn^{3+}-rich rows in the octahedral Mn layer leading to its orthogonal
588 symmetry (Fig. 9 in Gaillot et al. 2003; Fig. 6 in Marcus et al. 2004; Fig. 5 in Manceau et al.
589 2004; Manceau et al. 2005). To our knowledge, XRD patterns of all other turbostratic
590 varieties reported so far in the literature correspond to hexagonal modifications.

591 In addition Villalobos et al. (2006) demonstrated the high sensitivity of XRD profiles
592 to the layer and interlayer structure of turbostratic phyllomanganates. In their study,
593 Villalobos et al. (2006) observed contrasting experimental modulations of the 20,11 and 31,02
594 bands, and successfully reproduced them assuming a turbostratic stacking. In this case, the
595 position and profile of the bands depend essentially on the amount and atomic coordinates of
596 both layer and interlayer species, and these authors were able to determine the amount of
597 vacant layer sites, as well as the amount and coordinates of both "heavy" ($Mn^{3+,2+}$) and "light"
598 (Na^+, K^+, $H_2O_{interlayer}$) interlayer species. Such calculations also provided them with an
599 estimate of the lateral extension of the octahedral layers (Drits and Tchoubar 1990; Jurgensen
600 et al. 2004; Villalobos et al. 2006). The influence of the layer and interlayer structure on
601 calculated profiles for 20,11 and 31,02 bands is illustrated in Figure 13. As compared to the
602 structure model shown in Figure 12a (Model 1a), decreasing both the proportion of interlayer
603 Mn and layer vacancies from 0.167 to 0.075 broadens the lineshape of the 20,11 and
604 smoothes out the scattering dip at ~ 45° 2θ CuKα, thus rendering the calculated hump at ~50-
605 55° 2θ CuKα less pronounced (Fig. 12b). Moving interlayer Mn from the ^{VI}TC position
606 dramatically modifies the 20,11 lineshape, as observed when the 0.167 interlayer Mn atoms
607 are located above and/or below the tridentate cavities (^{VI}TE sites – Fig. 13c). The sensitivity
608 of the 20,11 profile to the position of "light" interlayer species is illustrated next by assuming
609 either the presence of Na^+ above and/or below O_{layer} [(0.333, 0.0, 0.5) – Fig. 13d] or that of K^+
610 above/below the tridentate cavities [Position (-0.222, 0, 05) and equivalent positions – Fig.
611 13e], H_2O molecules sitting in both cases above and/or below O_{layer}. In the second case, the
612 20,11 band is broadened and the "hump" observed at ~50° 2θ CuKα in Figure 13d is both
613 shifted towards higher angles and smoothened out. Similar modulations can however result
614 from the partial ordering of the layer stacking (e.g., Ben Brahim et al. 1983, 1984; Drits and
615 Tchoubar 1990; Viani et al. 2002). Special attention should thus be paid to the structural

616 interpretation of these modulations, and, in this respect, verifying the structural XRD model
617 with independent data from another structural technique, such as EXAFS spectroscopy, is
618 always warranted.
619
620 **ACKNOWLEDGMENTS**
621
622 VAD is grateful to the Environmental Geochemistry Group of the LGIT (Grenoble,
623 France) and to the Russian Science Foundation for financial support. VAD and BL
624 acknowledge financial support from CNRS/PICS709 program. The manuscript greatly
625 benefited from the remarks of two anonymous reviewers and from the editorial assistance of
626 AE Laurence Garvie.
627

REFERENCES CITED

Aronson, B.J., Kinser, A.K., Passerini, S., Smyrl, W.H., and Stein, A. (1999) Synthesis, characterization, and electrochemical properties of magnesium birnessite and zinc chalcophanite prepared by a low-temperature route. Chemistry of Materials, 11, 949-957.

Bach, S., Henry, M., Baffier, N., and Livage, J. (1990) Sol-gel synthesis of manganese oxides. Journal of Solid State Chemistry, 88, 325-333.

Bach, S., Pereira-Ramos, J.-P., and Bafier, N. (1993) Electrochemical sodium insertion into the sol-gel birnessite manganese dioxide. Electrochimica Acta, 38, 1695-1698.

Bailey, S.W. (1980) Structures of layer silicates. In G.W. Brindley, and G. Brown, Eds., Crystal Structures of Clay Minerals and their X-ray Identification, p. 1-123. Mineralogical Society, London.

-. (1988) Hydrous Phyllosilicates (exclusive of micas), 725 p. Mineralogical Society of America, Washington, D.C.

Bargar, J.R., Tebo, B.M., Bergmann, U., Webb, S.M., Glatzel, P., Chiu, V.Q., and Villalobos, M. (2005) Biotic and abiotic products of Mn(II) oxidation by spores of the marine *Bacillus sp.* strain SG-1. American Mineralogist, 90, 143-154.

Bartoli, C. (1997) Contribution à l'étude structurale des birnessites monocliniques saturées au potassium et au rubidium, 234 p. Ph.D. thesis, Orléans University, France.

Ben Brahim, J., Besson, G., and Tchoubar, C. (1983) Layer succession and water molecules arrangement in a homogeneous two-water layer Na-smectite. In J. Konta, Ed. 5th Meeting of the European Clay Groups, p. 65-75. Univerzita Karlova, Prague.

-. (1984) Etude des profils des bandes de diffraction X d'une beidellite-Na hydratée à deux couches d'eau. Détermination du mode d'empilement des feuillets et des sites occupés par l'eau. Journal of Applied Crystallography, 17, 179-188.

654 Bookin, A.S. and Drits, V.A. (1993) Polytype diversity of the hydrotalcite-like minerals. I.
655 Possible polytypes and their diffraction features. Clays & Clay Minerals, 41, 551-557.
656 Burns, R.G. and Burns, V.M. (1977) The mineralogy and crystal chemistry of deep-sea
657 manganese nodules, a polymetallic resource of the twenty-first century. Philosophical
658 Transactions of the Royal Society of London (A), 286, 283-301.
659 Burns, V.M. and Burns, R.G. (1978) Post-depositional metal enrichment processes inside
660 manganese nodules from the North Equatorial Pacific Ocean. Earth & Planetary
661 Science Letters, 39, 341-348.
662 Chao, T.T. and Theobald, P.K. (1976) The significance of secondary iron and manganese
663 oxides in geochemical exploration. Economic Geology, 71, 1560-1569.
664 Chen, R.J., Chirayil, T., Zavalij, P., and Whittingham, M.S. (1996a) The hydrothermal
665 synthesis of sodium manganese oxide and a lithium vanadium oxide. Solid State
666 Ionics, 86-88, 1-7.
667 Chen, R.J., Zavalij, P., and Whittingham, M.S. (1996b) Hydrothermal synthesis and
668 characterization of $K_xMnO_2.yH_2O$. Chemistry of Materials, 8, 1275-1280.
669 Ching, S., Landrigan, J.A., Jorgensen, M.L., Duan, N., Suib, S.L., and O'Young, C.L. (1995)
670 Sol-Gel synthesis of birnessite from $KMnO_4$ and simple sugars. Chemistry of
671 Materials, 7, 1604-1606.
672 Ching, S., Petrovay, D.J., Jorgensen, M.L., and Suib, S.L. (1997a) Sol-Gel Synthesis of
673 layered Birnessite-Type Manganese Oxides. Inorganic Chemistry, 36, 883-890.
674 Ching, S., Roark, J.L., Duan, N., and Suib, S.L. (1997b) Sol-Gel route to the tunneled
675 manganese oxide cryptomelane. Chemistry of Materials, 9, 750-754.
676 Ching, S. and Suib, S.L. (1997) Synthetic routes to microporous manganese oxides.
677 Comments on Inorganic Chemistry, 19, 263-282.

678 Cho, J., Kim, G.B., Lim, H.S., Kim, C.-S., and Yoo, S.-I. (1999) Improvement of Structural
679 Stability of $LiMn_2O_4$ Cathode Material on 55°C Cycling by Sol-Gel Coating of
680 $LiCoO_2$. Electrochemical and Solid-State Letters, 2, 607-609.
681 Chukhrov, F.V., Gorschkov, A.I., Rudnitskaya, E.S., and Sivtsov, A.V. (1978) Birnessite
682 characterization. Izvestiya Akademie Nauk, SSSR, Seriya Geologicheskaya, 9, 67-76.
683 Chukhrov, F.V., Sakharov, B.A., Gorshkov, A.I., Drits, V.A., and Dikov, Y.P. (1985) Crystal
684 structure of birnessite from the Pacific ocean. International Geology Review, 27,
685 1082-1088.
686 Cornell, R.M. and Giovanoli, R. (1988) Transformation of hausmannite into birnessite in
687 alkaline media. Clays & Clay Minerals, 36, 249-257.
688 Dachs, H. (1963) Neutronen- und Röntgenuntersuchungen am Manganit, MnOOH. Zeitschrift
689 für Kristallographie, 118, 303-326.
690 Delmas, C., Fouassier, C., and Hagenmuller, P. (1980) Structural classification and properties
691 of the layered oxides. Physica B, 99, 81-85.
692 Drits, V.A. (1987) Electron diffraction and high-resolution electron microscopy of mineral
693 structures, 304 p. Springer Verlag, Berlin Heidelberg.
694 Drits, V.A., Lanson, B., Bougerol Chaillout, C., Gorshkov, A.I., and Manceau, A. (2002)
695 Structure of heavy-metal sorbed birnessite: Part 2. Results from electron diffraction.
696 American Mineralogist, 87, 1646-1661.
697 Drits, V.A., Lanson, B., Gorshkov, A.I., and Manceau, A. (1998) Substructure and
698 superstructure of four-layer Ca-exchanged birnessite. American Mineralogist, 83, 97-
699 118.
700 Drits, V.A. and McCarty, D.K. (1996) The nature of diffraction effects from illite and illite-
701 smectite consisting of interstratified trans-vacant and cis-vacant 2:1 layers: A semi-

quantitative technique for determination of layer-type content. American Mineralogist, 81, 852-863.

Drits, V.A., Petrova, V.V., and Gorshkov, A.I. (1985) Manganese minerals of Fe-Mn nodules from the sediments of the central part of Pacific Ocean and their post-sedimentation transformation. Lithology and Raw Materials, 3, 17-39.

Drits, V.A., Silvester, E.J., Gorshkov, A.I., and Manceau, A. (1997a) The structure of monoclinic Na-rich birnessite and hexagonal birnessite. Part 1. Results from X-ray diffraction and selected area electron diffraction. American Mineralogist, 82, 946-961.

Drits, V.A., Srodon, J., and Eberl, D.D. (1997b) XRD measurement of mean crystallite tickness of illite and illite/smectite : Reappraisal of the Kubler index and the Scherrer equation. Clays and Clay Minerals, 45, 461-475.

Drits, V.A. and Tchoubar, C. (1990) X-ray diffraction by disordered lamellar structures: Theory and applications to microdivided silicates and carbons, 371 p. Springer-Verlag, Berlin.

Feng, Q., Kanoh, H., Miyai, Y., and Ooi, K. (1995) Hydrothermal synthesis of lithium and sodium manganese oxides and their metal ion extraction/insertion reactions. Chemistry of Materials, 7, 1226-1232.

Feng, Q., Sun, E.H., Yanagisawa, K., and Yamasaki, N. (1997a) Synthesis of birnessite-type sodium manganese oxides by solution reaction and hydrothermal methods. Journal of the Ceramic Society of Japan, 105, 564-568.

Feng, Q., Yanagisawa, K., and Yamasaki, N. (1997b) Synthesis of birnessite-type potassium manganese oxide. Journal of Materials Science Letters, 16, 110-112.

Gaillot, A.-C., Drits, V.A., Lanson, B., and Manceau, A. (2006a) Structure of synthetic K-rich birnessite obtained by high-temperature decomposition of KMnO4. Structure of a two-

726 layer polytype from 1000°C experiments. Microporous and Mesoporous Materials,
727 submitted.
728 Gaillot, A.-C., Drits, V.A., Plancon, A., and Lanson, B. (2004) Structure of synthetic K-rich
729 birnessites obtained by high-temperature decomposition of $KMnO_4$. 2. Phase and
730 structural heterogeneities. Chemistry of Materials, 16, 1890-1905.
731 Gaillot, A.-C., Flot, D., Drits, V.A., Manceau, A., Burghammer, M., and Lanson, B. (2003)
732 Structure of synthetic K-rich birnessite obtained by high-temperature decomposition
733 of $KMnO_4$. I. Two-layer polytype from 800 degrees C experiment. Chemistry of
734 Materials, 15, 4666-4678.
735 Gaillot, A.-C., Lanson, B., and Drits, V.A. (2005) Structure of birnessite obtained from
736 decomposition of permanganate under soft hydrothermal conditions. 1. Chemical and
737 structural evolution as a function of temperature. Chemistry of Materials, 17, 2959-
738 2975.
739 -. (2006b) Structure of birnessite obtained from decomposition of permanganate under soft
740 hydrothermal conditions. 2. Variation of the structure as a function of the nature of the
741 interlayer cation. Chemistry of Materials, in preparation.
742 Giovanoli, R., Stähli, E., and Feitknecht, W. (1970a) Über Oxidhydroxide des vierwertigen
743 Mangans mit Schichtengitter. 1. Mitteilung: Natriummangan(II,III)manganat(IV).
744 Helvetica Chimica Acta, 53, 209-220.
745 -. (1970b) Über Oxidhydroxide des vierwertigen Mangans mit Schichtengitter. 2. Mitteilung:
746 Mangan(III)-manganat(IV). Helvetica Chimica Acta, 53, 453-464.
747 Glasser, L.S.D. and Ingram, L. (1968) Refinement of the crystal structure of Groutite, α-
748 MnOOH. Acta Crystallographica, B24, 1233-1236.
749 Glover, E.D. (1977) Characterization of a marine birnessite. American Mineralogist, 62, 278-
750 285.

751 Golden, D.C., Dixon, J.B., and Chen, C.C. (1986) Ion exchange, thermal transformations, and
752 oxidizing properties of birnessite. Clays & Clay Minerals, 34, 511-520.
753 Gorshkov, A.I., Drits, V.A., Putilina, E.S., and Sivtsov, A.V. (1992) Natural and synthetic
754 birnessites. Lithology and raw materials, 6, 12-23.
755 Herbstein, H.F., Ron, G., and Weissman, A. (1971) The thermal decompoition of Potassium
756 Permanganate and related substances. Part I. Chemical aspects. Journal of the
757 Chemical Society (A), 1821-1826.
758 Jurgensen, A., Widmeyer, J.R., Gordon, R.A., Bendell Young, L.I., Moore, M.M., and
759 Crozier, E.D. (2004) The structure of the manganese oxide on the sheath of the
760 bacterium *Leptothrix discophora*: An XAFS study. American Mineralogist, 89, 1110-
761 1118.
762 Kim, S.H., Im, W.M., Hong, J.K., and Oh, S.M. (2000) Factors controlling the stability of O3-
763 and P2-type layered MnO_2 structures and spinel transition tendency in Li secondary
764 batteries. Journal of the Electrochemical Society, 147, 413-419.
765 Kim, S.H., Kim, S.J., and Oh, S.M. (1999) Preparation of layered MnO_2 via thermal
766 decomposition of $KMnO_4$ and its electrochemical characterizations. Chemistry of
767 Materials, 11, 557-563.
768 Kuma, K., Usui, A., Paplawsky, W., Gedulin, B., and Arrhenius, G. (1994) Crystal structures
769 of synthetic 7 Å and 10 Å manganates substituted by mono- and divalent cations.
770 Mineralogical Magazine, 58, 425-447.
771 Lanson, B., Drits, V.A., Feng, Q., and Manceau, A. (2002a) Structure of synthetic Na-
772 birnessite: Evidence for a triclinic one-layer unit cell. American Mineralogist, 87,
773 1662-1671.

774 Lanson, B., Drits, V.A., Gaillot, A.-C., Silvester, E., Plancon, A., and Manceau, A. (2002b)
775 Structure of heavy-metal sorbed birnessite: Part 1. Results from X-ray diffraction.
776 American Mineralogist, 87, 1631-1645.
777 Lanson, B., Drits, V.A., Silvester, E.J., and Manceau, A. (2000) Structure of H-exchanged
778 hexagonal birnessite and its mechanism of formation from Na-rich monoclinic
779 buserite at low pH. American Mineralogist, 85, 826-838.
780 Le Goff, P., Baffier, N., Bach, S., and Pereira-Ramos, J.-P. (1994) Structural and
781 electrochemical properties of layered manganese dioxides in relation to their
782 synthesis: Classical and sol-gel routes. Journal of Materials Chemistry, 4, 875-881.
783 -. (1996) Synthesis, ion exchange and electrochemical properties of lamellar
784 phyllomanganates of the birnessite group. Materials Research Bulletin, 31, 63-75.
785 Leroux, F., Guyomard, D., and Piffard, Y. (1995) The 2D rancieite-type manganic acid and its
786 alkali-exchanged derivatives: Part I - Chemical characterization and thermal behavior.
787 Solid State Ionics, 80, 299-306.
788 Ma, Y., Luo, J., and Suib, S.L. (1999) Syntheses of birnessites using alcohols as reducing
789 reagents: Effects of synthesis parameters on the formation of birnessites. Chemistry of
790 Materials, 11, 1972-1979.
791 Manceau, A. and Charlet, L. (1992) X-ray absorption spectroscopic study of the sorption of
792 Cr(III) at the oxide-water interface. Journal of Colloid and Interface Science, 148,
793 425-442.
794 Manceau, A., Drits, V.A., Lanson, B., Chateigner, D., Wu, J., Huo, D., Gates, W.P., and
795 Stucki, J.W. (2000a) Oxidation-reduction mechanism of iron in dioctahedral
796 smectites: II. Crystal chemistry of reduced Garfield nontronite. American
797 Mineralogist, 85, 153-172.

798 Manceau, A., Drits, V.A., Silvester, E.J., Bartoli, C., and Lanson, B. (1997) Structural
799 mechanism of Co^{2+} oxidation by the phyllomanganate buserite. American
800 Mineralogist, 82, 1150-1175.
801 Manceau, A., Gorshkov, A.I., and Drits, V.A. (1992a) Structural Chemistry of Mn, Fe, Co,
802 and Ni in Mn hydrous oxides. I. Information from XANES spectroscopy. American
803 Mineralogist, 77, 1133-1143.
804 -. (1992b) Structural Chemistry of Mn, Fe, Co, and Ni in Mn hydrous oxides. II. Information
805 from EXAFS spectroscopy, electron and X-ray diffraction. American Mineralogist,
806 77, 1144-1157.
807 Manceau, A., Lanson, B., and Drits, V.A. (2002) Structure of heavy metal sorbed birnessite.
808 Part III: Results from powder and polarized extended X-ray absorption fine structure
809 spectroscopy. Geochimica Et Cosmochimica Acta, 66, 2639-2663.
810 Manceau, A., Lanson, B., Drits, V.A., Chateigner, D., Gates, W.P., Wu, J., Huo, D., and
811 Stucki, J.W. (2000b) Oxidation-reduction mechanism of iron in dioctahedral
812 smectites: I. Crystal chemistry of oxidized reference nontronites. American
813 Mineralogist, 85, 133-152.
814 Manceau, A., Lanson, B., Schlegel, M.L., Harge, J.-C., Musso, M., Eybert Berard, L.,
815 Hazemann, J.-L., Chateigner, D., and Lamble, G.M. (2000c) Quantitative Zn
816 speciation in smelter-contaminated soils by EXAFS spectroscopy. American Journal
817 of Science, 300, 289-343.
818 Manceau, A., Marcus, M.A., Tamura, N., Proux, O., Geoffroy, N., and Lanson, B. (2004)
819 Natural speciation of Zn at the micrometer scale in a clayey soil using X-ray
820 fluorescence, absorption, and diffraction. Geochimica Et Cosmochimica Acta, 68,
821 2467-2483.

822 Manceau, A., Schlegel, M.L., Chateigner, D., Lanson, B., Bartoli, C., and Gates, W.P. (1999)
823 Application of polarized EXAFS to fine-grained layered minerals. In D.G. Schulze,
824 J.W. Stucki, and P.M. Bertsch, Eds., Synchrotron X-ray methods in clay science, 9, p.
825 68-114. Clay Minerals Society, Boulder, Co.
826 Manceau, A., Tommaseo, C., Rihs, S., Geoffroy, N., Chateigner, D., Schlegel, M., Tisserand,
827 D., Marcus, M.A., Tamura, N., and Chen, Z.S. (2005) Natural speciation of Mn, Ni,
828 and Zn at the micrometer scale in a clayey paddy soil using X-ray fluorescence,
829 absorption, and diffraction. Geochimica Et Cosmochimica Acta, 69, 4007-4034.
830 Mandernack, K.W., Post, J., and Tebo, B.M. (1995) Manganese mineral formation by
831 bacterial spores of the marine *Bacillus*, strain SG-1: Evidence for the direct oxidation
832 of Mn(II) to Mn(IV). Geochimica Et Cosmochimica Acta, 59, 4393-4408.
833 Marcus, M.A., Manceau, A., and Kersten, M. (2004) Mn, Fe, Zn and As speciation in a fast-
834 growing ferromanganese marine nodule. Geochimica Et Cosmochimica Acta, 68,
835 3125-3136.
836 Méring, J. (1949) L'interférence des rayons-X dans les systèmes à stratification désordonnée.
837 Acta Crystallographica, 2, 371-377.
838 Norrestam, R. (1967) α-Manganese (III) oxide - A C-type sesquioxide of orthorhombic
839 symmetry. Acta Chemica Scandinavica, 21, 2871-2884.
840 Paterson, E., Swaffield, R., and Clark, L. (1994) The influence of structure on Ba and K
841 uptake by a synthetic phyllomangante. Clay Minerals, 29, 215-222.
842 Plançon, A. (2002) CALCIPOW- a program for calculating the diffraction by disordered
843 lamellar structures. Journal of Applied Crystallography, 35, 377.
844 Post, J.E. and Veblen, D.R. (1990) Crystal structure determinations of synthetic sodium,
845 magnesium, and potassium birnessite using TEM and the Rietveld method. American
846 Mineralogist, 75, 477-489.

847 Shannon, R.D. (1976) Revised effective ionic radii and systematic studies of interatomic
848 distances in halides and chalcogenides. Acta Crystallographica, A32, 751-767.
849 Shannon, R.D., Gumeman, P.S., and Chenavas, J. (1975) Effect of octahedral distortion on
850 mean Mn^{3+}-O distances. American Mineralogist, 60, 714-716.
851 Silvester, E.J., Manceau, A., and Drits, V.A. (1997) The structure of monoclinic Na-rich
852 birnessite and hexagonal birnessite. Part 2. Results from Chemical Studies and
853 EXAFS Spectroscopy. American Mineralogist, 82, 962-978.
854 Stone, A.T., Godtfredsen, K.L., and Deng, B. (1994) Sources and reactivity of reductant
855 encountered in aquatic environments. In G. Bidoglio, and W. Stumm, Eds., Chemistry
856 of aquatic systems: Local and global perspectives, p. 337-374. ECSC, EEC, EAEC,
857 Brussels.
858 Tebo, B.M., Bargar, J.R., Clement, B.G., Dick, G.J., Murray, K.J., Parker, D., Verity, R., and
859 Webb, S.M. (2004) Biogenic manganese oxides: Properties and mechanisms of
860 formation. Annual Review of Earth and Planetary Sciences, 32, 287-328.
861 Tebo, B.M. and He, L.M. (1999) Microbially mediated oxidative precipitation reactions. In
862 D.L. Sparks, and T.J. Grundl, Eds., Mineral-water interfacial reactions, 715, p. 393-
863 414. American Chemical Society, Washington, D.C.
864 Töpfer, J., Trari, M., Gravereau, P., Chaminade, J.P., and Doumerc, J.P. (1995) Crystal
865 growth and reinvestigation of the crystal structure of crednerite, $CuMnO_2$. Zeitschrift
866 für Kristallographie, 210, 184-187.
867 Tsuji, M., Komarneni, S., Tamaura, Y., and Abe, M. (1992) Cation exchange properties of a
868 layered manganic acid. Materials Research Bulletin, 27, 741-751.
869 Tu, S., Racz, G.J., and Goh, T.B. (1994) Transformations of synthetic birnessite as affected
870 by pH and manganese concentration. Clays & Clay Minerals, 42, 321-330.

871 Viani, A., Gaultieri, A.F., and Artioli, G. (2002) The nature of disorder in montmorillonite by
872 simulation of X-ray powder patterns. American Mineralogist, 87, 966-975.
873 Villalobos, M., Lanson, B., Manceau, A., Toner, B., and Sposito, G. (2006) Structural model
874 for the biogenic Mn oxide produced by Pseudomonas putida. American Mineralogist,
875 91, 489-502.
876 Villalobos, M., Toner, B., Bargar, J., and Sposito, G. (2003) Characterization of the
877 manganese oxide produced by Pseudomonas putida strain MnB1. Geochimica Et
878 Cosmochimica Acta, 67, 2649-2662.
879 Webb, S.M., Tebo, B.M., and Bargar, J.R. (2005) Structural characterization of biogenic Mn
880 oxides produced in seawater by the marine *Bacillus sp*. strain SG-1. American
881 Mineralogist, 90, 1342-1357.
882 Yang, D.S. and Wang, M.K. (2001) Syntheses and characterization of well-crystallized
883 birnessite. Chemistry of Materials, 13, 2589-2594.
884

885 **FIGURE CAPTIONS**

886

887 **FIGURE 1.** Idealized structure model of birnessite polytypes. **a)** 1*H* polytype. Top: projection
888 along the **b** axis. Open and solid symbols indicate atoms at $y = 0$ and $y = \pm ½$,
889 respectively. Large circles represent O_{layer} atoms and small circles represent Mn_{layer},
890 atoms. Dashed lines outline specific positions of the close-packing formalism.
891 Irregular dashed lines outline the interlayer octahedra defined by O_{layer} from adjacent
892 layers. Bottom: projection on the **ab** plane. The upper surface of the lower layer is
893 shown as light shaded triangles whereas the lower surface of the upper layer is
894 shown as dark shaded triangles. Mn_{layer} of the upper layer are shown as small open
895 circles. **b)** $2H_1$ polytype. Top: projection along the **b** axis. Irregular dashed lines
896 outline the interlayer prisms defined by O_{layer} from adjacent layers. Bottom:
897 projection on the **ab** plane. Mn_{layer} of the lower layer are shown as small solid circles.
898 Other symbols as in Figure 1a. **c)** $2H_2$ polytype. Top: projection along the **b** axis.
899 Irregular dashed lines outline the interlayer octahedra defined by O_{layer} from adjacent
900 layers. Bottom: projection on the **ab** plane. Symbols and notations as in Figure 1a.

901 **FIGURE 2.** Idealized structure model of birnessite polytypes in projection along the **b** axis. **a)**
902 $3R_1$ polytype. Symbols and notations as in Figure 1. Irregular dashed lines outline the
903 interlayer prisms defined by O_{layer} from adjacent layers. **b)** $3R_2$ polytype. Symbols
904 and notations as in Figure 1. Irregular dashed lines outline the interlayer octahedra
905 defined by O_{layer} from adjacent layers. **c)** $3H_1$ polytype. Symbols and notations as in
906 Figure 1. Irregular dashed lines as in Figure 2b. **d)** $3H_2$ polytype. Symbols and
907 notations as in Figure 1. Irregular dashed lines as in Figure 2b.

908 **FIGURE 3.** Idealized interlayer structure model in projection along the **b** axis for birnessite
909 polytypes with layer vacancies (hexagonal layer symmetry). **a)** 1*H* polytype with

910 octahedrally coordinated cations above/below vacant layer sites (^{VI}TC position –
911 Model 1a). Symbols and notations as in Figure 1. Irregular dashed lines outline the
912 interlayer prisms defined by $H_2O_{interlayer}$ coordinating the interlayer cations and O_{layer}
913 from adjacent layers (H-bonds). **b)** $3R_1$, $3R_2$ and $2H_1$ polytypes with octahedrally
914 coordinated cations above/below vacant layer sites (^{VI}TC position – Models 2a, 3a
915 and 4a, respectively). Symbols and notations as in Figure 1. Irregular dashed lines
916 outline the interlayer octahedra defined by $H_2O_{interlayer}$ coordinating the interlayer
917 cations and O_{layer} from adjacent layers (weak H-bonds). **c)** $2H_2$, $3H_1$ and $3H_2$
918 polytypes with octahedrally coordinated cations above/below vacant layer sites (^{VI}TC
919 position – Models 5a, 6a and 7a, respectively). Irregular dashed lines outline the
920 interlayer prisms (left) and octahedra defined by $H_2O_{interlayer}$ coordinating the
921 interlayer cations and O_{layer} from adjacent layers (strong and weak H-bonds,
922 respectively). **d)** $3R_2$ polytype with tetrahedrally coordinated cations above/below
923 vacant layer sites (^{IV}TC position – Model 3b). Irregular dashed line outlines the
924 strong H-bond between $H_2O_{interlayer}$ coordinating the interlayer cation and O_{layer} from
925 adjacent layers.

926 **FIGURE 4.** Idealized interlayer structure model in projection along the **b** axis for birnessite
927 polytypes with vacancy-free layers (orthogonal layer symmetry). **a)** $1M_2$ polytype
928 with octahedrally coordinated cations above/below empty layer tetrahedra (tridentate
929 cavities) sharing three edges with layer Mn octahedra (^{VI}TE position – Model 3d).
930 Symbols and notations as in Figure 1. Irregular dashed lines outline the interlayer
931 prisms defined by $H_2O_{interlayer}$ coordinating the interlayer cations and O_{layer} from
932 adjacent layers (H-bonds). **b)** $1O$ and $2O_1$ polytypes with octahedrally coordinated
933 cations above/below empty layer tetrahedra (tridentate cavities) sharing three edges
934 with layer Mn octahedra (^{VI}TE position – Models 1b and 4d, respectively). Symbols

and notations as in Figure 1. Irregular dashed lines outline the interlayer octahedra defined by $H_2O_{interlayer}$ coordinating the interlayer cations and O_{layer} from adjacent layers (weak H-bonds).

FIGURE 5. XRD patterns calculated for idealized structure models of birnessite polytypes. **a)** 1*H* polytype with $Mn^{3+,2+}$ in ^{VI}TC position (Model 1a). **b)** $3R_1$ polytype with $Mn^{3+,2+}$ in ^{VI}TC position (Model 2a). **c)** $3R_2$ polytype with Zn^{2+} in ^{VI}TC position (Model 3a). **d)** $2H_1$ polytype with $Mn^{3+,2+}$ in ^{VI}TC position (Model 4a). **e)** $2H_2$ polytype with $Mn^{3+,2+}$ in ^{VI}TC position (Model 5a). f) $3H_1$ polytype with $Mn^{3+,2+}$ in ^{VI}TC position (Model 6a). **g)** $3H_2$ polytype with $Mn^{3+,2+}$ in ^{VI}TC position (Model 7a).

XRD patterns were calculated using the idealized structure models described in Table 3. *a* and *b* unit-cell parameters for the polytypes having a hexagonal layer symmetry are 4.936 and 2.850 Å, respectively, whereas they are 5.180 and 2.850 Å, respectively, for the polytypes having a orthogonal layer symmetry. In all cases the minimum periodicity along the **c*** axis is 7.10 Å. All calculations were performed assuming a periodic stacking mode devoid of random stacking faults. The radius of the coherent scattering domains in the **ab** plane was set to 150 Å for all calculations, whereas the mean extent of the coherent scattering domains perpendicular to the layer plane is 7 layers (maximum extent: 35 layers). The distribution of coherent scattering domain size along the **c*** axis was assumed to be lognormal (Drits et al. 1997b). The values of Debye-Waller thermal factor (B) were 0.5, 1.0 and 1.5 for Mn_{layer}, O_{layer} and $H_2O_{interlayer}$, respectively. B factors for $Me_{interlayer}$ were either 1.0 (metal cations Zn^{2+}, $Mn^{3+,2+}$, …) or 2.0 (alkali and alkali-earth cations: K^+, Ca^{2+}, …).

FIGURE 6. XRD patterns calculated for idealized structure models of birnessite $3R_2$ polytype. **a)** With Zn^{2+} in ^{IV}TC position (Model 3b). **b)** With Zn^{2+} in ^{VI}TC position (Model 3a). **c)** With Zn^{2+} in ^{IV}TE position (Model 3c).

960 **FIGURE 7.** XRD patterns calculated for idealized structure models of birnessite polytypes. **a)**
961 $1M_2$ polytype with K^+ in the interlayer mid-plane (Model 3e). **b)** $1M_2$ polytype with
962 Ca^{2+} in ^{VI}TE sites (Model 3d). **c)** $2O_1$ polytype with K^+ in the interlayer mid-plane
963 (Model 4c). **d)** $2O_1$ polytype with Ca^{2+} in ^{VI}TE sites (Model 4d).

964 **FIGURE 8.** XRD patterns calculated for idealized structure models of birnessite polytypes. **a)**
965 $3R_1$ polytype with K^+ in the interlayer mid-plane (Model 2b). **b)** $3R_1$ polytype with
966 $Mn^{3+,2+}$ in ^{VI}TC position (Model 2a). **c)** $2H_1$ polytype with K^+ in the interlayer mid-
967 plane (Model 4b). **d)** $2H_1$ polytype with $Mn^{3+,2+}$ in ^{VI}TC position (Model 4a).

968 **FIGURE 9.** XRD patterns calculated for idealized structure models of birnessite polytypes. **a)**
969 $2H_2$ polytype with $Mn^{3+,2+}$ in ^{VI}TC position (Model 5a). **b)** $2H_1$ polytype with $Mn^{3+,2+}$
970 in ^{VI}TC position (Model 4a). **c)** $2O_1$ polytype with K^+ in the interlayer mid-plane
971 (Model 4c).

972 **FIGURE 10.** XRD patterns calculated for idealized structure models of birnessite polytypes. **a)**
973 $3R_1$ polytype with K^+ in the interlayer mid-plane (Model 2b). **b)** $3R_2$ polytype with
974 Zn^{2+} in ^{VI}TC position (Model 3a). **c)** $3H_1$ polytype with $Mn^{3+,2+}$ in ^{VI}TC position
975 (Model 6a). **d)** $3H_2$ polytype with $Mn^{3+,2+}$ in ^{VI}TC position (Model 7a).

976 **FIGURE 11.** Comparison between experimental and calculated XRD patterns for a K-rich
977 birnessite sample synthesized at 700°C from the thermal decomposition of $KMnO_4$
978 (Gaillot et al. 2004). Experimental data are shown as crosses, whereas calculated
979 profiles are shown as solid lines. Arrows outline the misfits between experimental
980 and calculated patterns. Only 20*l* and 11*l* reflections are calculated. Atomic
981 coordinates and other structural parameters used for the calculations as described by
982 (Gaillot et al. 2004). (a) Optimum model and difference plot. The optimum model
983 includes contributions from a defect-free 2*H* polytype and from 2*O*/2*H*, 2*H*/3*R*, and
984 3*R*/2*H* mixed-layered structures (relative proportions 7:29:41:23). (b) Calculation

made replacing the optimum 2*O*/2*H* contribution (2*O*:2*H* ratio 50:50) by a defect-free 2*H* contribution. (c) Calculation made by subtracting the 2*H*/3*R* contribution (2*H*:3*R* ratio 70:30) from the optimum model. (d) Calculation made by subtracting the 3*R*/2*H* contribution (3*R*:2*H* ratio 90:10) from the optimum model. Adapted from (Gaillot et al. 2004).

FIGURE 12. XRD patterns calculated for idealized structure models of turbostratic birnessite. **a)** Birnessite with $Mn^{3+,2+}$ in ^{VI}TC position (Model 1a). **b)** Birnessite with 0.67 Na^+ and $H_2O_{interlayer}$ in the interlayer mid-plane above below O_{layer} (Model 2c).

Calculations were performed assuming a turbostratic stacking (100% random stacking faults). The radius of the coherent scattering domains in the **ab** plane was set to 75 Å. All other parameters for XRD pattern calculations as described for Figure 5.

FIGURE 13. XRD patterns calculated for idealized structure models of turbostratic birnessite having hexagonal layer symmetry. **a)** Birnessite with 0.833 vacant layer sites capped by $Mn^{3+,2+}$ in ^{VI}TC position (Model 1a). **b)** Birnessite with 0.925 vacant layer sites capped by $Mn^{3+,2+}$ in ^{VI}TC position. **c)** Birnessite with 0.833 vacant layer sites capped by $Mn^{3+,2+}$ in ^{VI}TE position (similar to Model 3d with interlayer $Mn^{3+,2+}$ cations). **d)** Birnessite with 0.925 vacant layer sites and interlayer Na^+ (0.30 per octahedron) and H_2O molecules (0.90 per octahedron) in c' position (+1/3, 0, 1/2). **e)** Birnessite with 0.925 vacant layer sites and interlayer K^+ (0.30 per octahedron) in and H_2O molecules (0.90 per octahedron) in a' (-0.222, 0, 1/2) and c' (+1/3, 0, 1/2) positions, respectively.

Calculations were performed as described for Figure 12.

Table 1. List of possible periodic layer stacking modes in birnessite consisting of hexagonal (vacancy-bearing) or orthogonal (vacancy-free) layers

Layer stacking	Hexagonal layers	Orthogonal layers
AbC – AbC …	1*H*	1*O*
AbC = CbA = AbC …	$2H_1$	$2O_1$
AbC – AcB – AbC …	$2H_2$	$2O_2$
AbC = CaB = BcA = AbC …	$3R_1$	$1M_1$
AbC – BcA – CaB – AbC …	$3R_2$	$1M_2$
AbC – AcB – AcB – AbC …	$3H_1$	$3O_1$
AbC – AcB – CaB – AbC …	$3H_2$	$3O_2$

Table 2. Symbolic notations of birnessite consisting of hexagonal (vacancy-bearing) and orthogonal (vacancy-free) layers and differing from each other by stacking modes and interlayer structures.

Hexagonal layer symmetry				Layers with orthogonal symmetry			
Polyt.	Model	XRD (fig.)	Notation	Polyt.	Model	XRD (fig.)	Notation
1*H*	1a	5a	$AbC_{b'A,}\ ^{C'b'}AbC\ldots$	1*O*	1b		$AbC_{a'B,}\ ^{B'c'}AbC\ldots$
3R_1	2a	5b, 8b	$AbC_{b'A,}\ ^{B'a'}CaB_{a'C,}\ ^{A'c'}BcA_{c'B,}\ ^{C'b'}AbC\ldots$	1M_1	2c		AbC c' CaB b' BcA a' AbC…
3R_1	2b	8a, 10a	AbC b'/a' CaB a'/c' BcA c'/b' AbC…		2d		$AbC_{a'A,}\ ^{B'b'}CaB_{c'C,}\ ^{A'a'}BcA_{b'B,}\ ^{C'c'}AbC\ldots$
3R_2	3a	6b, 10b	$AbC_{b'A,}\ ^{A'c'}BcA_{c'B,}\ ^{B'a'}CaB_{a'C,}\ ^{C'b'}AbC\ldots$	1M_2	3d	7b	$AbC_{a'B,}\ ^{C'a'}BcA_{b'C,}\ ^{A'b'}CaB_{c'A,}\ ^{B'c'}AbC\ldots$
3R_2	3b	5c, 6a	$AbC_{b'B,}\ ^{C'c'}BcA_{c'C,}\ ^{A'a'}CaB_{a'A,}\ ^{B'b'}AbC\ldots$	1M_2	3e	7a	AbC a' BcA b' CaB c' AbC…
3R_2	3c	6c	$AbC_{a'A,}\ ^{A'a'}BcA_{b'B,}\ ^{B'b'}CaB_{c'C,}\ ^{C'c'}AbC\ldots$				
2H_1	4a	5d, 8d, 9b	$AbC_{b'A,}\ ^{A'b'}CbA_{b'C,}\ ^{C'b'}AbC\ldots$	2O_1	4c	7c, 9c	AbC a' CbA c' AbC…
2H_1	4b	8c	AbC a'/C' CbA c'/A' AbC…	2O_1	4d	7d	$AbC_{a'B,}\ ^{B'a'}CbA_{c'B,}\ ^{B'c'}AbC\ldots$
		5e, 9a		2O_1	4e		AbC c' CbA a' AbC…
2H_2	5a		$AbC_{b'A,}\ ^{B'c'}AcB_{c'A,}\ ^{C'b'}AbC\ldots$	2O_2	5d		$AbC_{a'B,}\ ^{C'b'}AcB_{a'C,}\ ^{B'c'}AbC\ldots$

$2H_2$	5b		AbC b' AcB c' AbC…	$2O_2$	5e	$AbC_{a'A'}{}^{C'b'}AcB_{a'A'}{}^{B'c'}AbC…$
$2H_2$	5c		$AbC_{b'A'}{}^{C'c'}AcB_{c'A'}{}^{B'b'}AbC…$			
$3H_1$	6a	5f, 10c	$AbC_{b'A'}{}^{B'c'}AcB_{c'A'}{}^{B'c'}AcB_{c'A'}{}^{C'b'}AbC…$			
$3H_1$	6b	5g, 10d	AbC b' AcB c' AcB c' AbC…			
$3H_2$	7a		$AbC_{b'A'}{}^{B'c'}AcB_{c'A'}{}^{B'a'}CaB_{a'C'}{}^{C'b'}AbC…$			

Table 3. Atomic positions and site occupancies for the idealized structure models described in Table 2.

Model		1a	2a	2b
Polytype		1*H*	3R_1	3R_1
XRD pattern	Fig.	5a	5b, 8b	8a
Mn_{layer}	x[a]	0	0	0
	y[a]	0	0	0
	ζ[b]	0	0	0
	occ	0.833	0.833	0.925
O_{layer}	x[a]	+/-0.333	+/-0.333	+/-0.333
	y[a]	0	0	0
	ζ[b]	+/-1.00	+/-1.00	+/-1.00
	Occ	1 x 2	1 x 2	1 x 2
Cat. Inter.	Type	Mn	Mn	K
	x[a]	0.000	0.000	0
	y[a]	0	0	0
	ζ[b]	+/-2.15	+/-2.15	+/-3.55
	Occ	0.0833 x2	0.0833 x2	0.15 x2
H_2O	x[a]	-/+0.333	-/+0.333	+/-0.333
	y[a]	0	0	0
	ζ[b]	+/-3.35	+/-3.35	+/-3.55
	Occ	0.250 x2	0.250 x2	0.300 x2
Interlayer shift		0.0	-0.333*a*	-0.333*a*

Notes: [a]x and y atomic positions are expressed in fraction of ideal C-centered unit-cell *a* and *b* parameters, respectively. x positions are given in projection normal to the **ab** plane. [b]Position ζ along *c* is expressed in Å to emphasize the thickness of layer and interlayer polyhedra. Occupancy (occ) is given as the sum of all equivalent sites.

Table 3. (continued).

Model		3a	3b	3c	3d	3e
Polytype		$3R_2$	$3R_2$	$3R_2$	$1M_2$	$1M_2$
XRD pattern	Fig.	8b, 10b	5c, 6a	6c	7b	7a
Mn_{layer}	x[a]	0	0	0	0	0
	y[a]	0	0	0	0	0
	ζ[b]	0	0	0	0	0
	Occ	0.833	0.833	0.833	0.833	1.000
O_{layer}	x[a]	+/-0.333	+/-0.333	+/-0.333	+/-0.333	+/-0.333
	y[a]	0	0	0	0	0
	ζ[b]	+/-1.00	+/-1.00	+/-1.00	+/-1.00	+/-1.00
	Occ	2	2	2	2	2
Cat. Inter.	Type	Zn	Zn	Zn	Ca	K
	x[a]	0.000	0.000	-/+0.333	-/+0.333	-/+0.333
	y[a]	0	0	0	0	0
	ζ[b]	+/-2.20	+/-1.77	+/-1.77	+/-2.30	+/-3.55
	Occ	0.0833 x2	0.0833 x2	0.0833 x2	0.0833 x2	0.150 x2
H_2O[c]	x[a]	-/+0.333	0	-/+0.333	0	-/+0.333
	y[a]	0	0	0	0	0
	ζ[b]	+/-3.55	+/-3.70	+/-3.70	+/-3.70	+/-3.55
	Occ	0.250 x2	0.0833 x2	0.0833 x2	0.250 x2	0.300 x2
Int. shift		+0.333*a*	+0.333*a*	+0.333*a*	+0.333*a*	+0.333*a*

Table 3. (continued).

Model		4a	4b	4c	4d	5a
Polytype		$2H_1$	$2H_1$	$2O_1$	$2O_1$	$2H_2$
XRD pattern	Fig.	5d, 8d, 9b, 10d	8c	7c	7d	5e, 9a
Mn_{layer}	x[a]	0	0	0	0	0
	y[a]	0	0	0	0	0
	ζ[b]	0	0	0	0	0
	Occ	0.833	0.925	1.000	1.000	0.833
O_{layer}	x[a]	+/-0.333	+/-0.333	+/-0.333	+/-0.333	+/-0.333
	y[a]	0	0	0	0	0
	ζ[b]	+/-1.00	+/-1.00	+/-1.00	+/-1.00	+/-1.00
	Occ	2	2	2	2	2
Cat. Inter.	Type	Mn	K	K	Ca	Mn
	x[a]	0.000	-0.222 0.111/0.111	-0.222 0.111/0.111	-/+0.333	0
	y[a]	0	0 +/-0.333	0 +/-0.333	0	0
	ζ[b]	+/-2.15	3.55	3.55	+/-2.30	+/-2.15
	Occ	0.0833 x2	0.100 x3	0.100 x3	0.0833 x2	0.0833 x2
H_2O[c]	x[a]	-/+0.333	0.333	0.333	0	-/+0.333
	y[a]	0	0	0	0	0
	ζ[b]	+/-3.35	+3.55	+3.55	+/-3.70	+/-3.35
	Occ	0.250 x2	0.600	0.600	0.250 x2	0.250 x2
Mn_{layer}	x[a]	0	0	0	0	0.333
	y[a]	0	0	0	0	0
	ζ[b]	7.10	7.10	7.10	7.10	7.10
	Occ	0.833	0.925	1.000	1.000	0.833
O_{layer}	x[a]	+/-0.333	+/-0.333	+/-0.333	+/-0.333	-0.333/0.000
	y[a]	0	0	0	0	0
	ζ[b]	6.10/8.10	6.10/8.10	6.10/8.10	6.10/8.10	6.10/8.10
	Occ	2	2	2	2	2
Cat. Inter.	Type	Mn	K	K	Ca	Mn
	x[a]	0.000	0.222 -0.111/-0.111	0.222 -0.111/-0.111	-/+0.333	0.333
	y[a]	0	0 +/-0.333	0 +/-0.333	0	0
	ζ[b]	4.95/9.25	10.65	10.65	4.80/9.40	4.95/9.25
	Occ	0.0833 x2	0.100 x3	0.100 x3	0.0833 x2	0.0833 x2
H_2O[c]	x[a]	-/+0.333	-0.333	-0.333	0	0.000/-0.333
	y[a]	0	0	0	0	0
	ζ[b]	3.75/10.45	10.65	10.65	3.40/10.80	3.75/10.45
	Occ	0.250 x2	0.600	0.600	0.250 x2	0.250 x2
Int. shift		0	0	0	0	0

Table 3. (continued).

Model		6a	7a
Polytype		$3H_1$	$3H_2$
XRD pattern	Fig.	5f, 10c	5g
Mn_{layer}	x[a]	0	0
	y[a]	0	0
	ζ[b]	0	0
	occ	0.833	0.833
O_{layer}	x[a]	+/-0.333	+/-0.333
	y[a]	0	0
	ζ[b]	+/-1.00	+/-1.00
	occ	2	2
Cat. Inter.	Type	Mn	Mn
	x[a]	0	0
	y[a]	0	0
	ζ[b]	+/-2.15	+/-2.15
	occ	0.0833 x2	0.0833 x2
H_2O[c]	x[a]	-/+0.333	-/+0.333
	y[a]	0	0
	ζ[b]	+/-3.35	+/-3.35
	occ	0.250 x2	0.250 x2
Mn_{layer}	x[a]	0.333	0.333
	y[a]	0	0
	ζ[b]	7.10	7.10
	occ	0.833	0.833
O_{layer}	x[a]	-0.333/0.000	-0.333/0.000
	y[a]	0	0
	ζ[b]	6.10/8.10	6.10/8.10
	occ	2	2
Cat. Inter.	Type	Mn	Mn
	x[a]	0.333	0.333
	y[a]	0	0
	ζ[b]	4.95/9.25	4.95/9.25
	occ	0.0833 x2	0.0833 x2
H_2O[c]	x[a]	0.000/-0.333	0.000/-0.333
	y[a]	0	0
	ζ[b]	3.75/10.45	3.75/10.45
	occ	0.250 x2	0.250 x2
Mn_{layer}	x[a]	0.333	-0.333
	y[a]	0	0
	ζ[b]	14.20	14.20
	occ	0.833	0.833
O_{layer}	x[a]	-0.333/0.000	0.333/0.000
	y[a]	0	0
	ζ[b]	13.20/15.20	13.20/15.20
	occ	2	2
Cat. Inter.	Type	Mn	Mn
	x[a]	0.333	-0.333
	y[a]	0	0
	ζ[b]	12.05/16.35	12.05/16.35
	occ	0.0833 x2	0.0833 x2
H_2O[c]	x[a]	0.000/-0.333	0.000/0.333
	y[a]	0	0
	ζ[b]	10.85/17.55	10.85/17.55
	occ	0.250 x2	0.250 x2
Int. shift		0	0

Table 4A. Calculated d(*hkl*) values for birnessite polytypes consisting of vacancy-bearing layers having a hexagonal layer symmetry (See Table 1).

Polytype	1*H*	2*H*	3*R*/3*H*
d(*hkl*)	*hkl*	*hkl*	*hkl*
2.468	200,110	200,110	200,110
2.452	-	-	201,111
2.432	-	201,111	-
2.404	-	-	202,112
2.331	201,111	202,112	203,113
2.239	-	-	204,114
2.188	-	203,113	-
2.136	-	-	205,115
2.026	202,112	204,114	206,116
1.917	-	-	207,117
1.863		205,115	-
1.810	-	-	208,118
1.708	203,113	206,116	209,119
1.613	-	-	20.10,11.10
1.567		207,117	-
1.523	-	-	20.11,11.11
1.441	204,114	208,118	20.12,11.12
1.425	020,310	020,310	020,310
1.422	-	-	021,311
1.418	-	021,311	-
1.412	-	-	022,312
1.397	021,311	022,312	023,313
1.376	-	-	024,314
1.365	-	-	20.13,11.13
1.364	-	023,313	-
1.351	-	-	025,315
1.329	-	209,119	-
1.322	022,312	024,314	026,316
1.295	-	-	20.14, 11.14
1.290	-	-	027,317
1.274	-	025,315	-
1.256	-	-	028,318
1.231	-	20.10,11.10	20.15,11.15
1.221	023,313	026,316	029,319

Notes: a and *b* unit-cell parameters are 4.936, and 2.850 Å, respectively. The minimum periodicity along the **c*** axis is 7.10 Å for all polytypes.

Table 4B. Calculated d(*hkl*) values for birnessite polytypes consisting of vacancy-free layers having an orthogonal layer symmetry (See Table 1)

Polytype	1*O*	1M_1	1M_2	2O_1/2O_2
d(*hkl*)	*Hkl*	*hkl*	*Hkl*	*hkl*
2.590	200			200
2.571		20-1	201	
2.548				201/20-1
2.517		200	200	
2.497	110			110
2.480		110	110	
2.459				111/11-1
2.433	201/20-1			202/20-2
2.431		11-1	111	
2.356	111/11-1			112/11-2
2.329		20-2	202	
2.272				203/20-3
2.261		111	11-1	
2.214		201	20-1	
2.209				113/11-3
2.154		11-2	112	
2.092	202/20-2			204/20-4
2.042	112/11-2			114/11-4
1.972		20-3	203	
1.930		112	11-2	
1.914				205/20-5
1.875				115/11-5
1.857		202	20-2	
1.821		11-3	113	
1.747	203/20-3			206/20-6
1.718	113/11-3			116/11-6
1.645		20-4	204	
1.621		113	11-3	
1.597				207/20-7
1.574				117/11-7
1.551		203	20-3	
1.530		11-4	114	
1.477	310	31-1	311	310
1.469				311/31-1
1.464	204/20-4			208/20-8
1.447	114/11-4			118/11-8
1.446	311/31-1	310/31-2	310/312	312/31-2
1.425	020	020	020	020
1.418				021/02-1
1.410				313/31-3
1.397	021/02-1	021/02-1	021/02-1	022/02-2
1.384		20-5	205	
1.370		114	11-4	
1.365				023/02-3
1.364	312/31-2	311	31-1	314/31-4
1.363		31-3	313	
1.347				209/20-9
1.334				119/11-9
1.322	022/02-2	022/02-2	022/02-2	024/02-4
1.312		204	20-4	
1.310				315/31-5
1.299		11-5	115	
1.274				025/02-5
1.253	313/31-3	312/31-4	314/31-2	316/31-6
1.245	205/20-5			20.10/20.-10
1.234	115/11-5			11.10/11.-10

1.221	023/02-3	023/02-3	023/02-3	026/02-6

Notes: a and *b* unit-cell parameters are 5.180 and 2.850 Å, respectively. The minimum periodicity along the **c*** axis is 7.10 Å for all polytypes. The β angle is 103.65 and 76.35° for $1M_1$ and $1M_2$ polytypes, respectively.

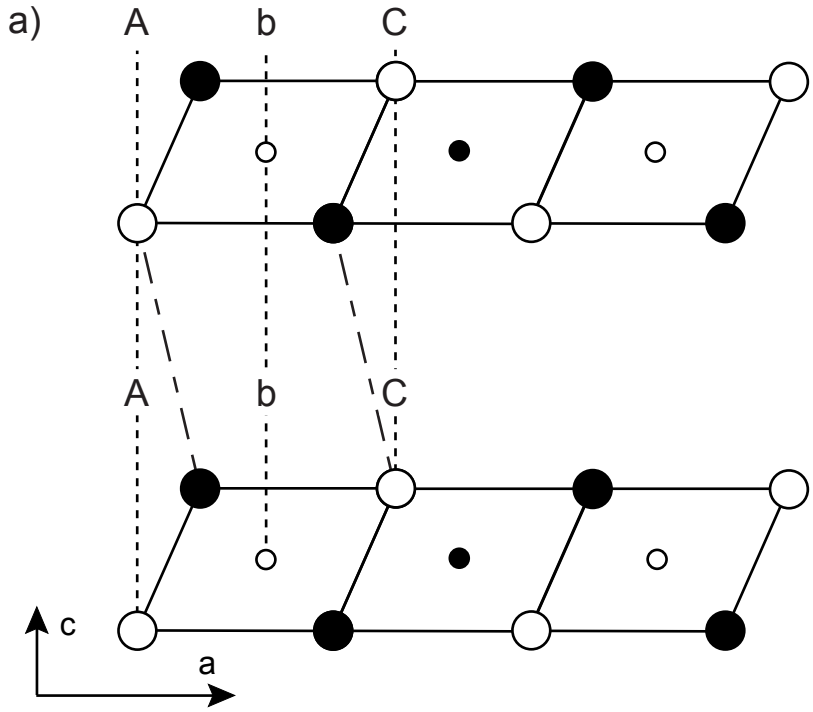

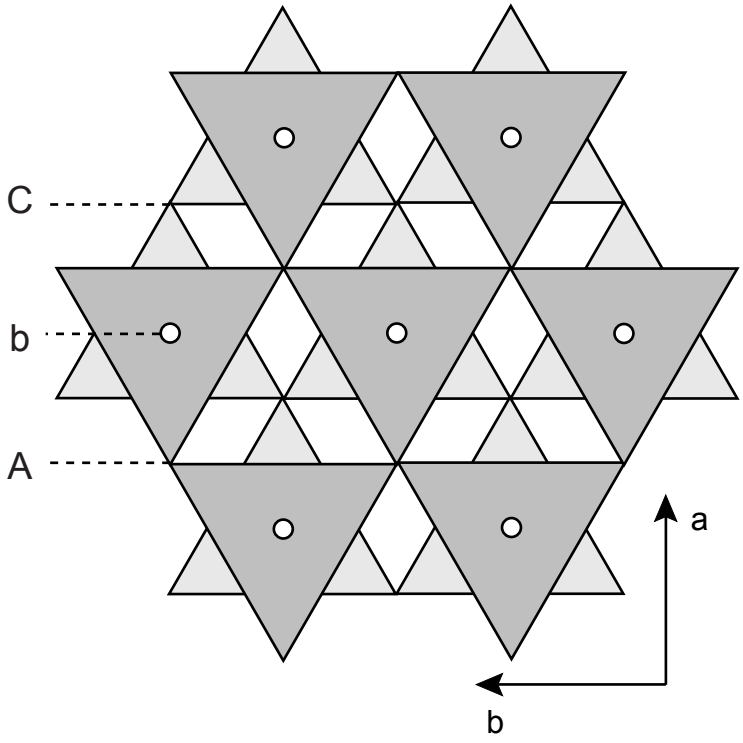

Drits et al. Fig. 01

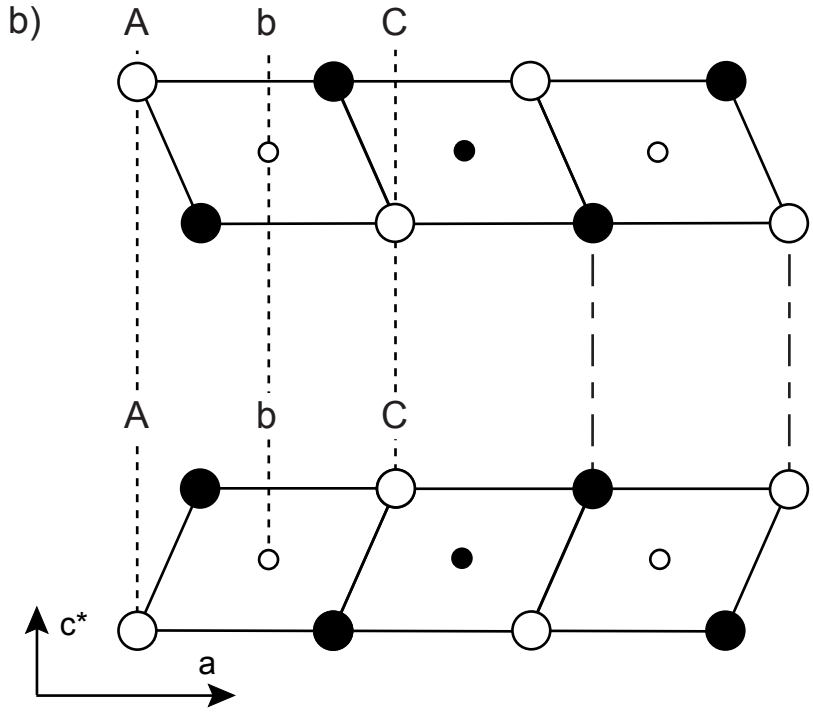

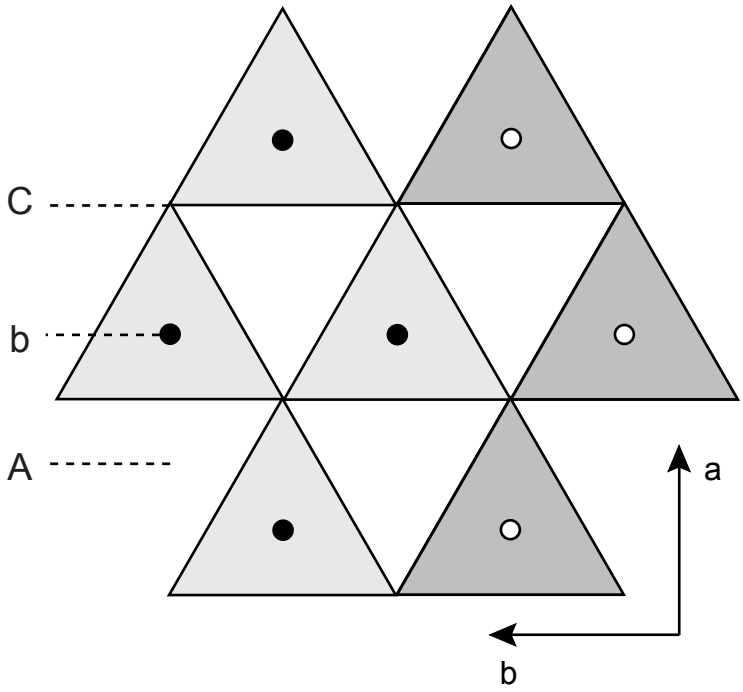

Drits et al. Fig. 01

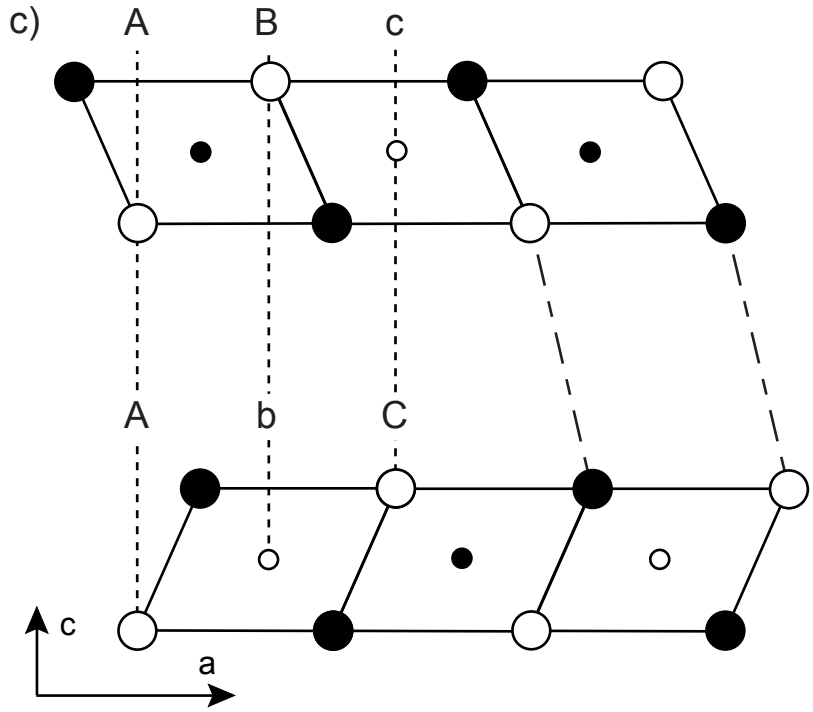

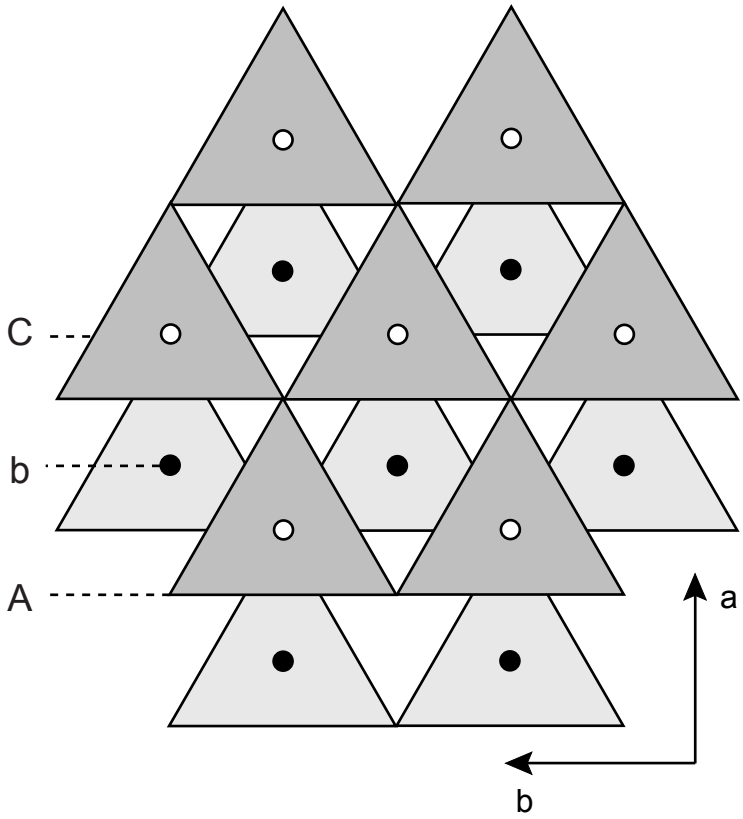

Drits et al. Fig. 01

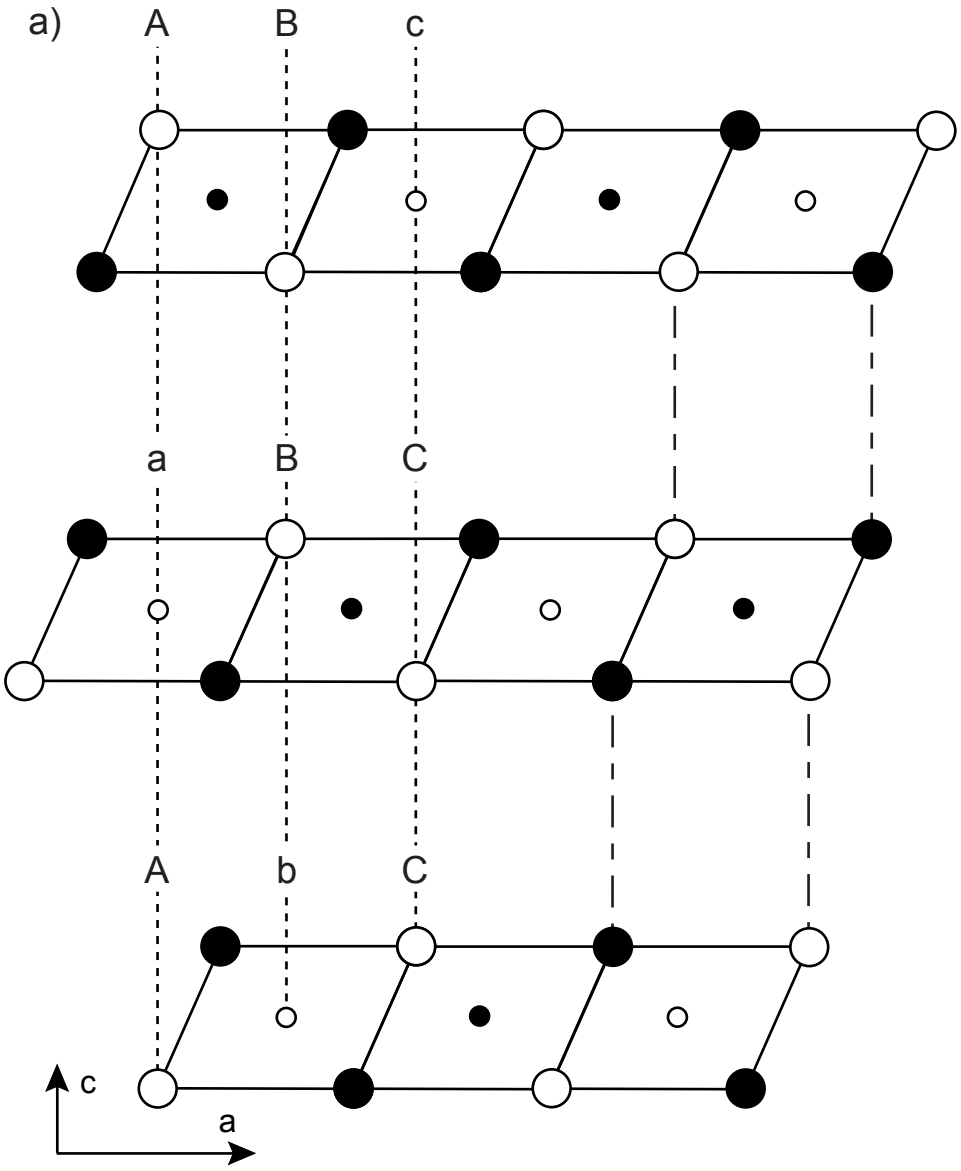

Drits et al. Fig. 02

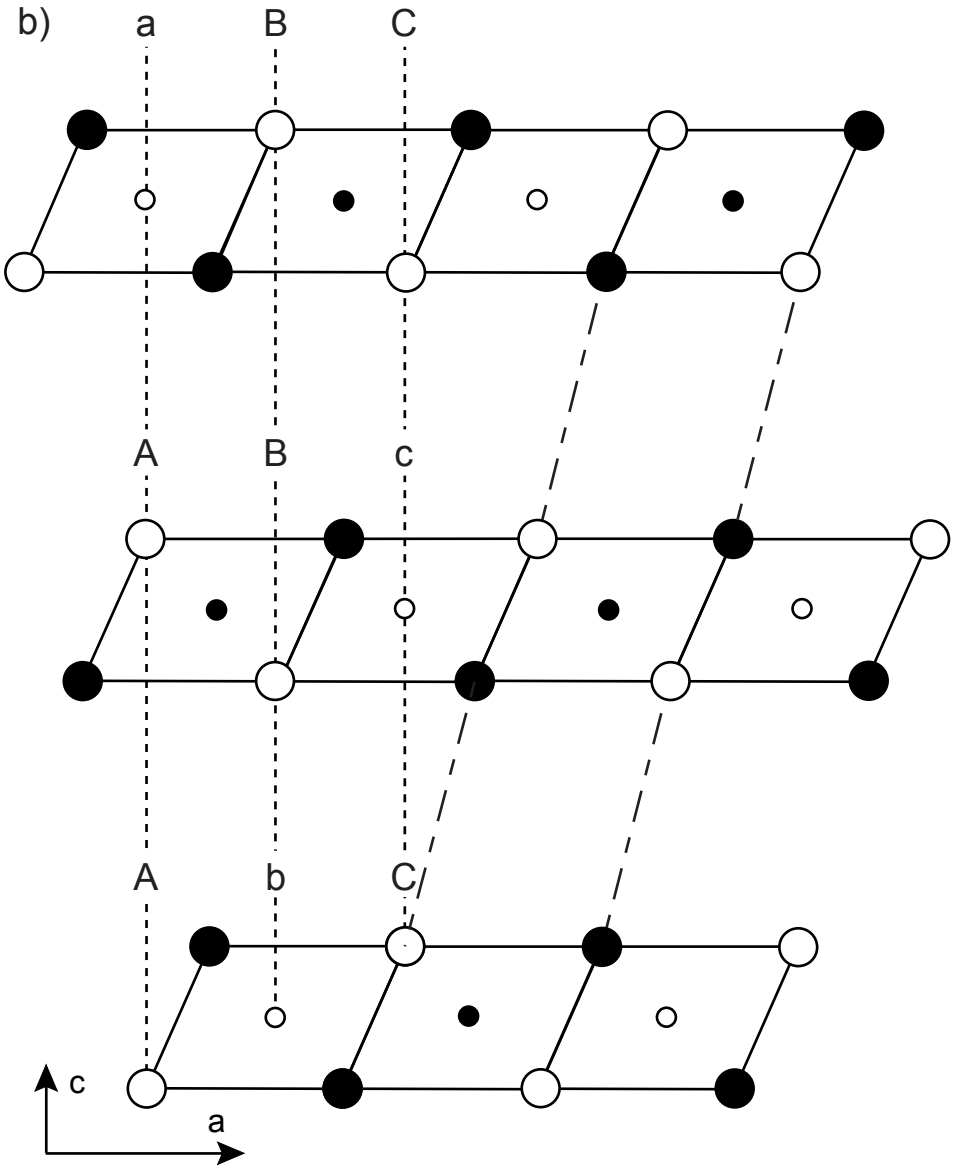

Drits et al. Fig. 02

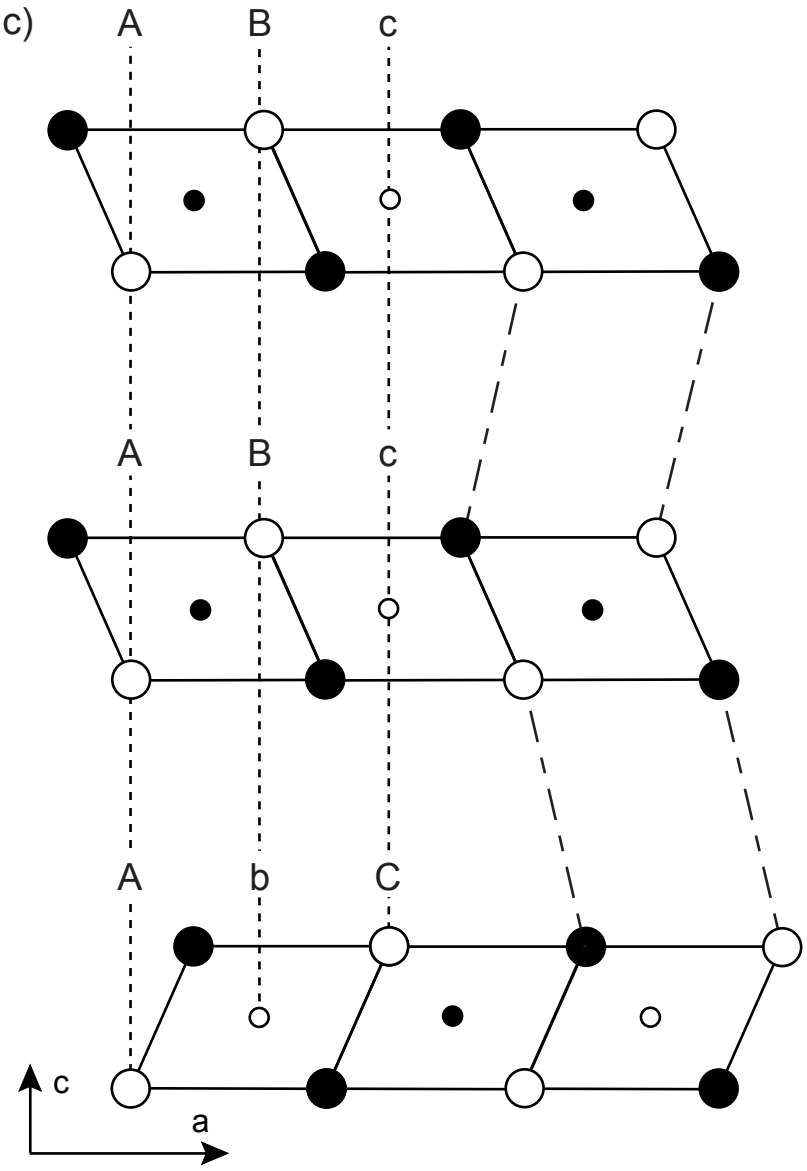

Drits et al. Fig. 02

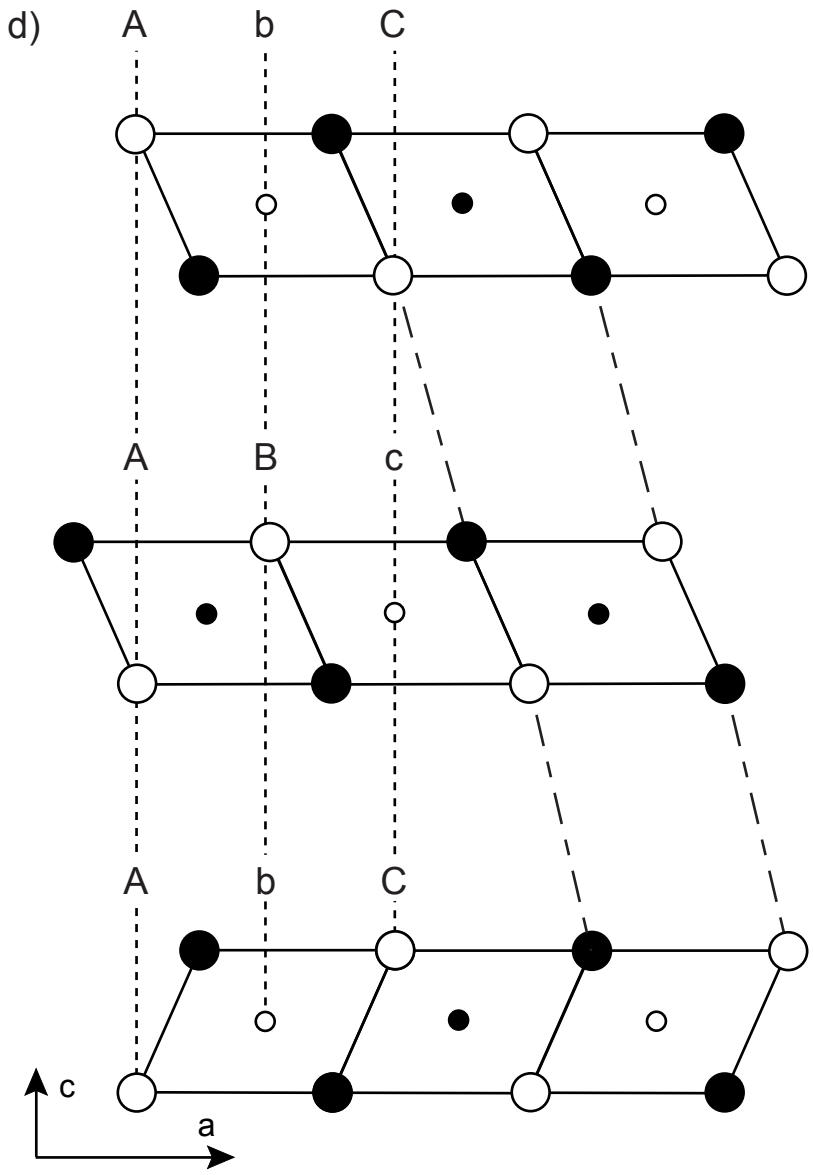

Drits et al. Fig. 02

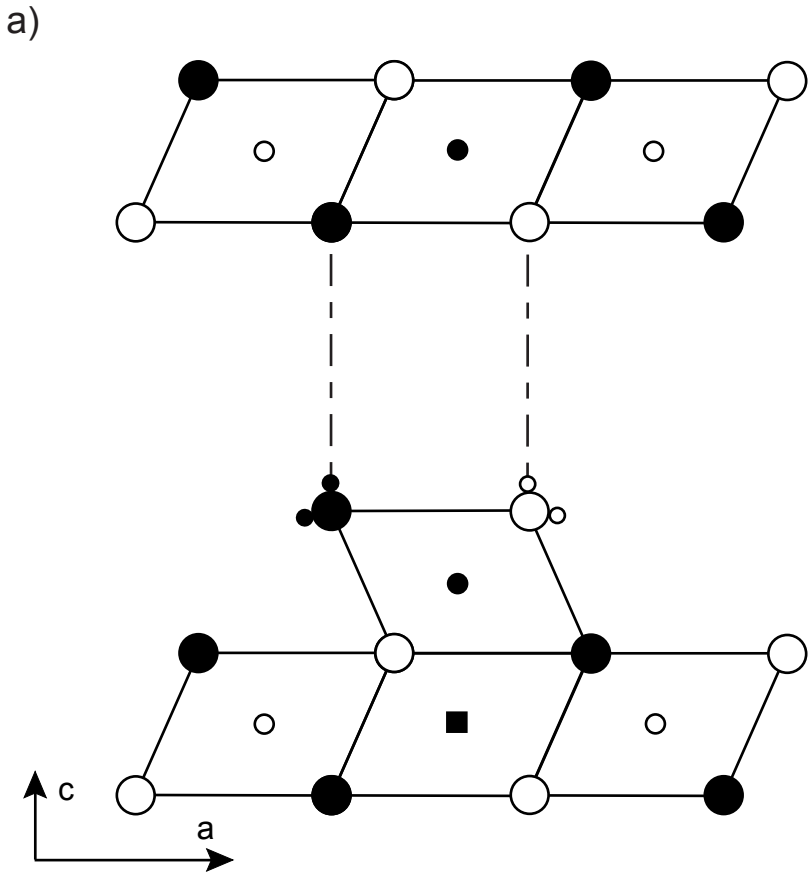

Drits et al. Fig. 03

b)

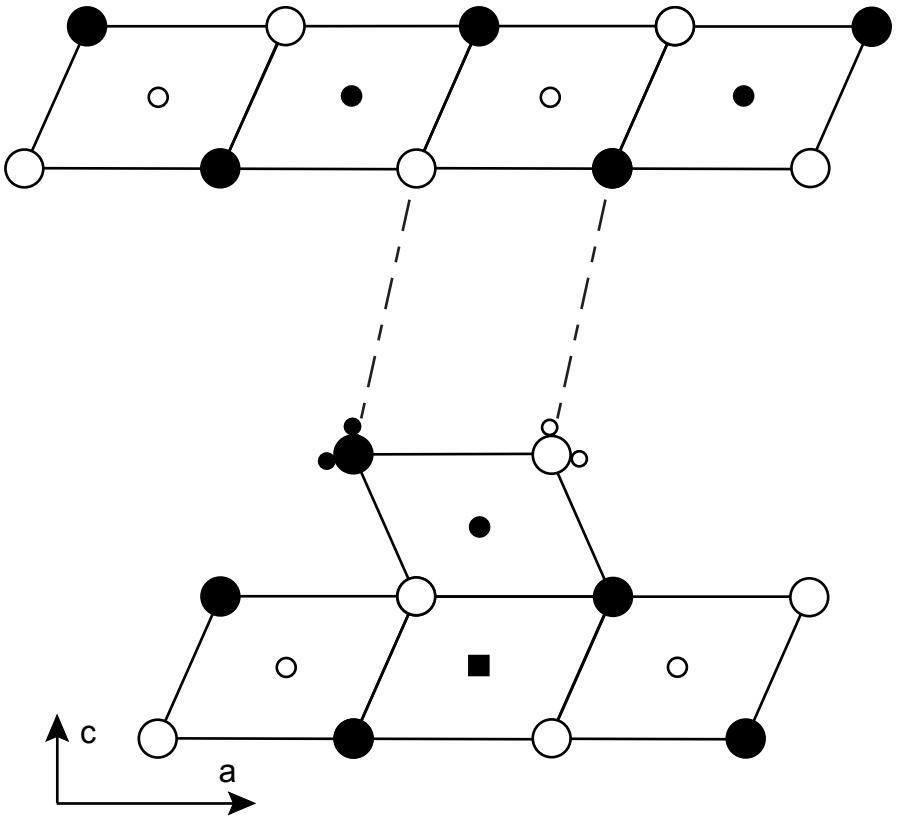

Drits et al. Fig. 03

c)

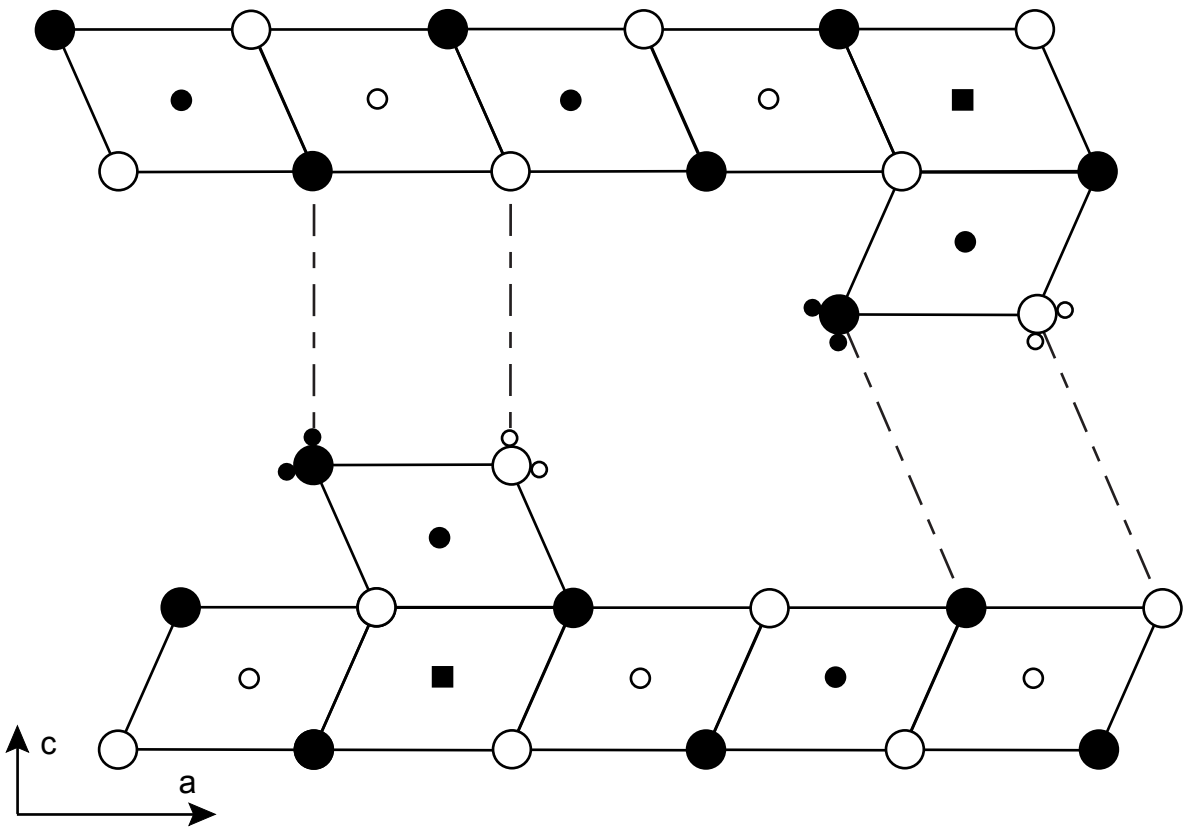

Drits et al. Fig. 03

d)

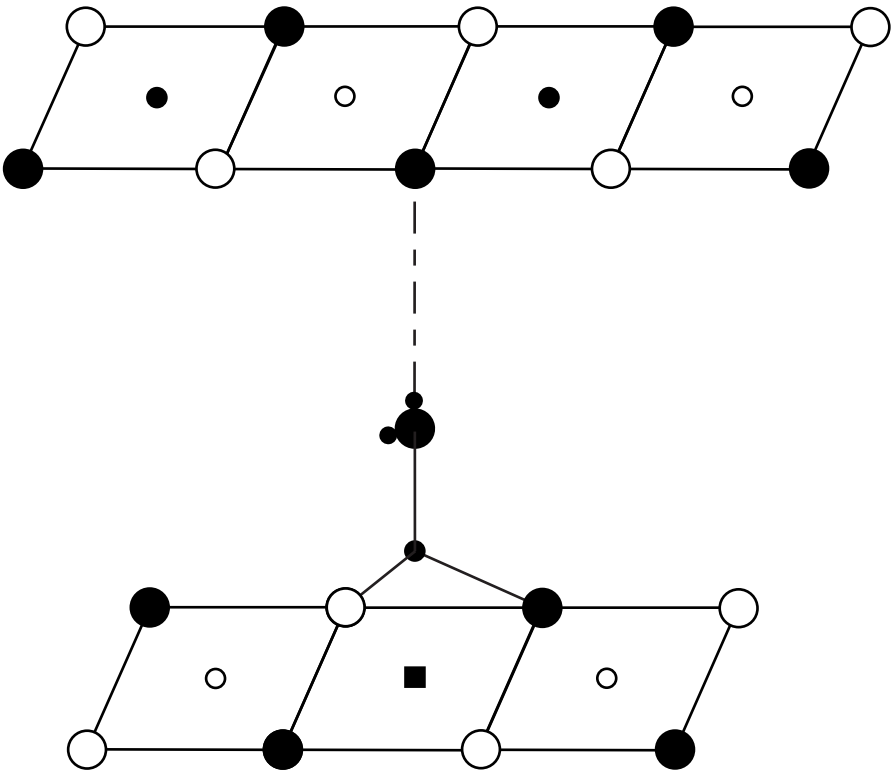

Drits et al. Fig. 03

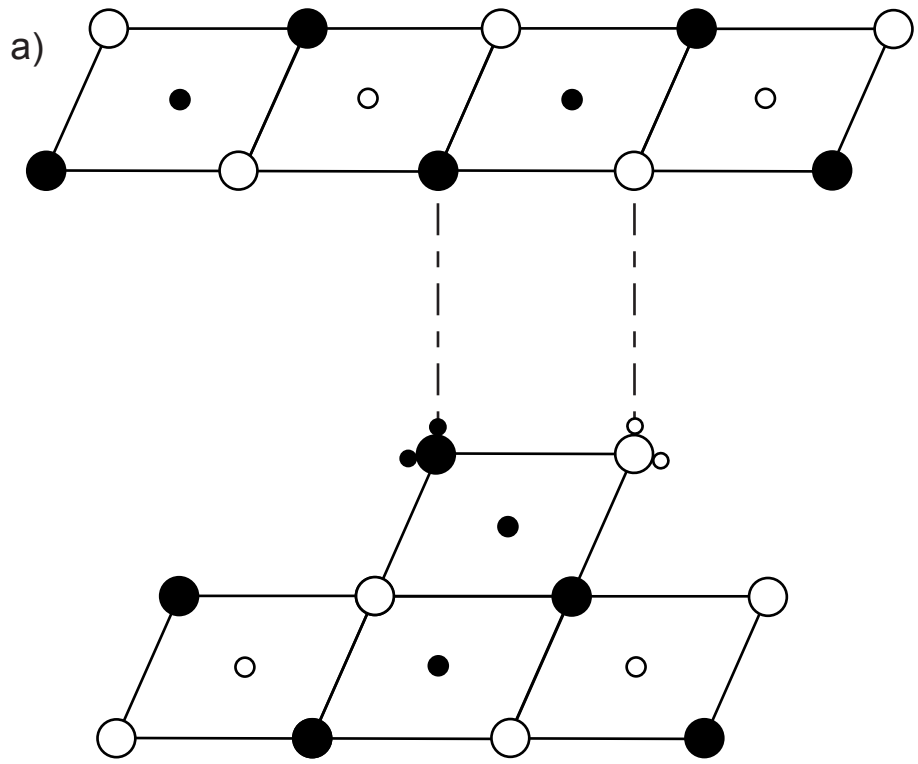

Drits et al. Fig. 04

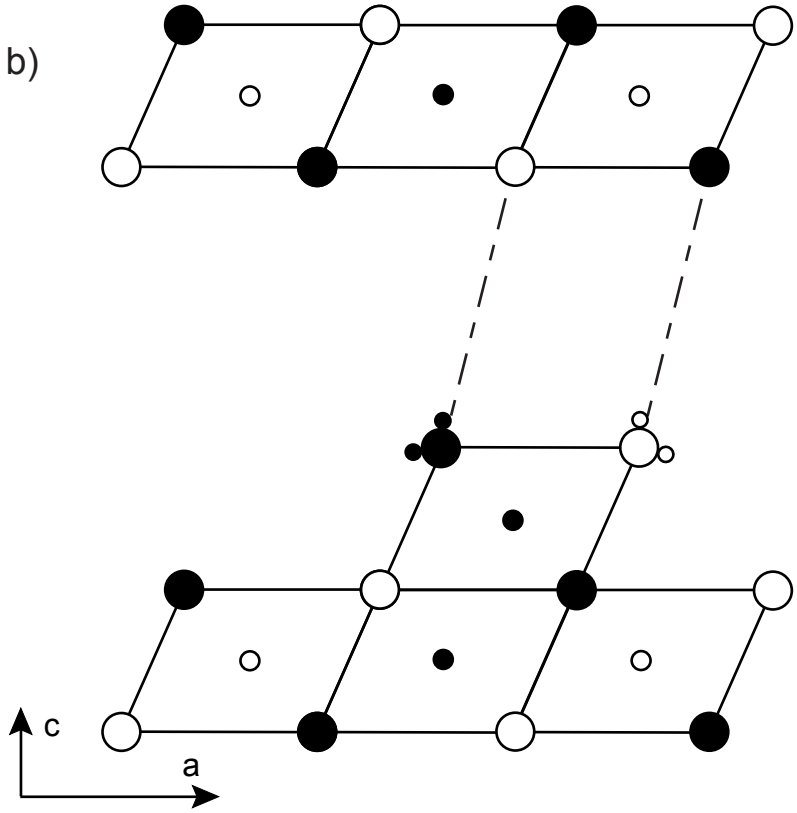

Drits et al. Fig. 04

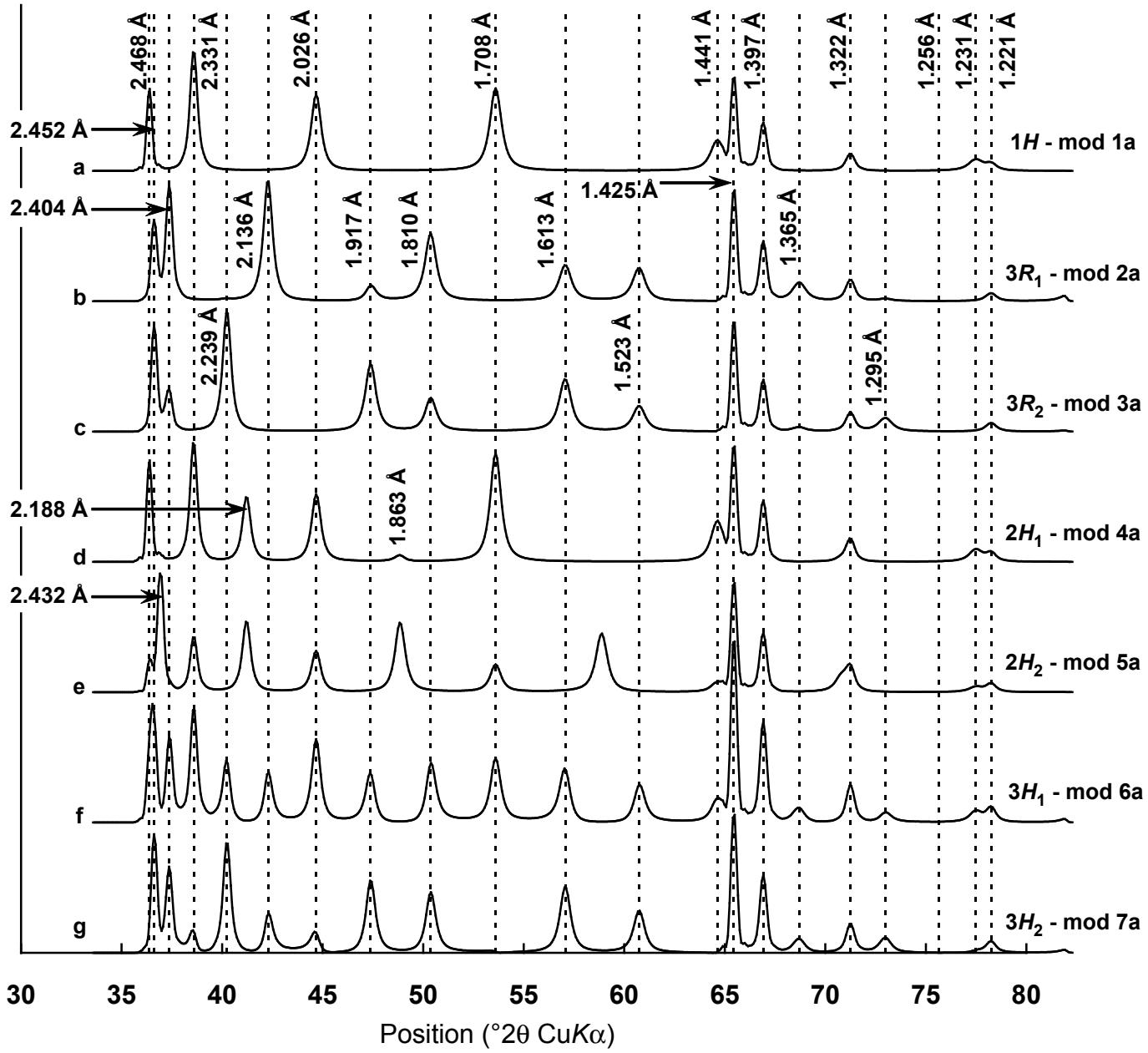

Drits et al. Fig. 05

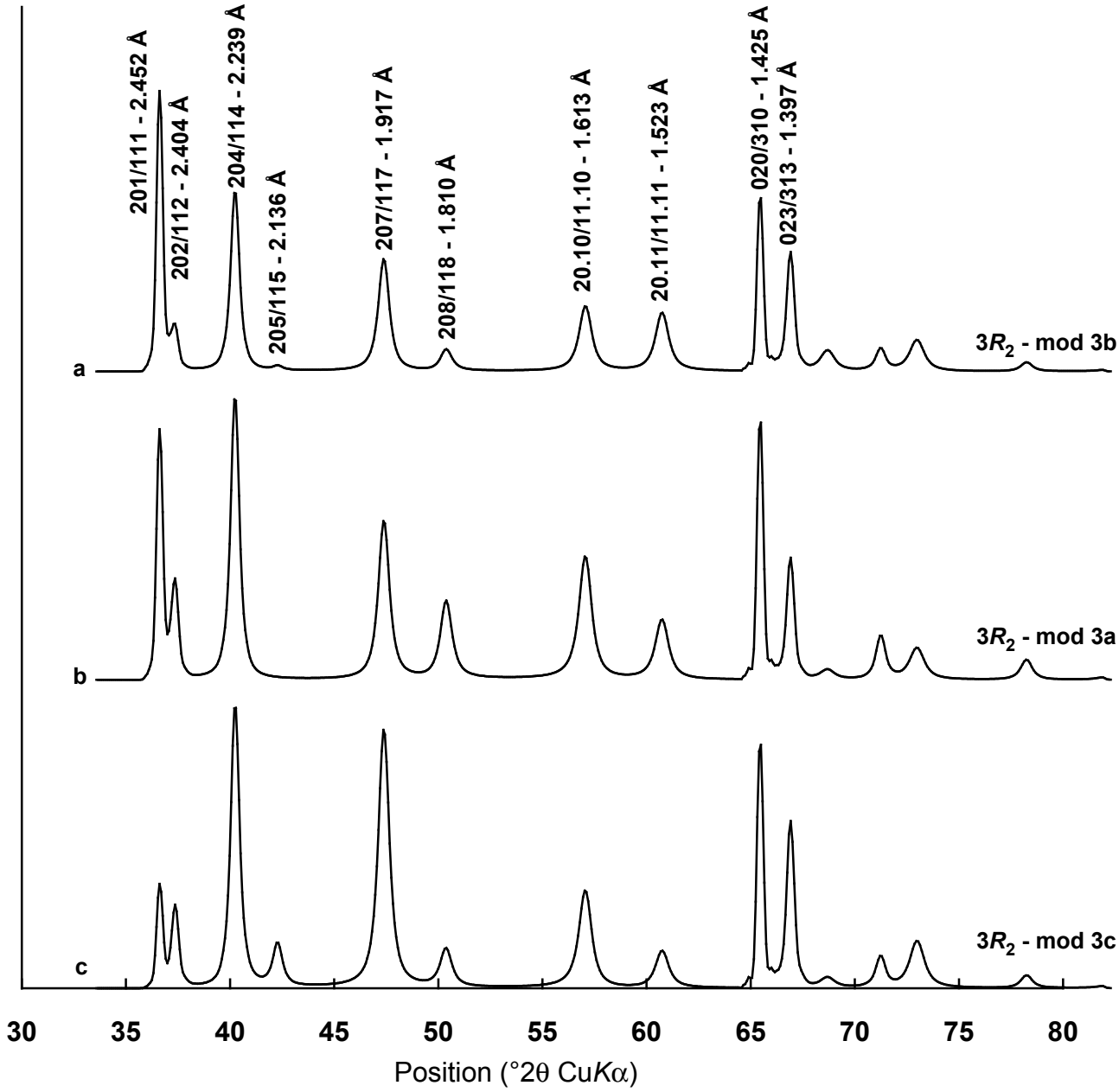

Drits et al. Fig. 06

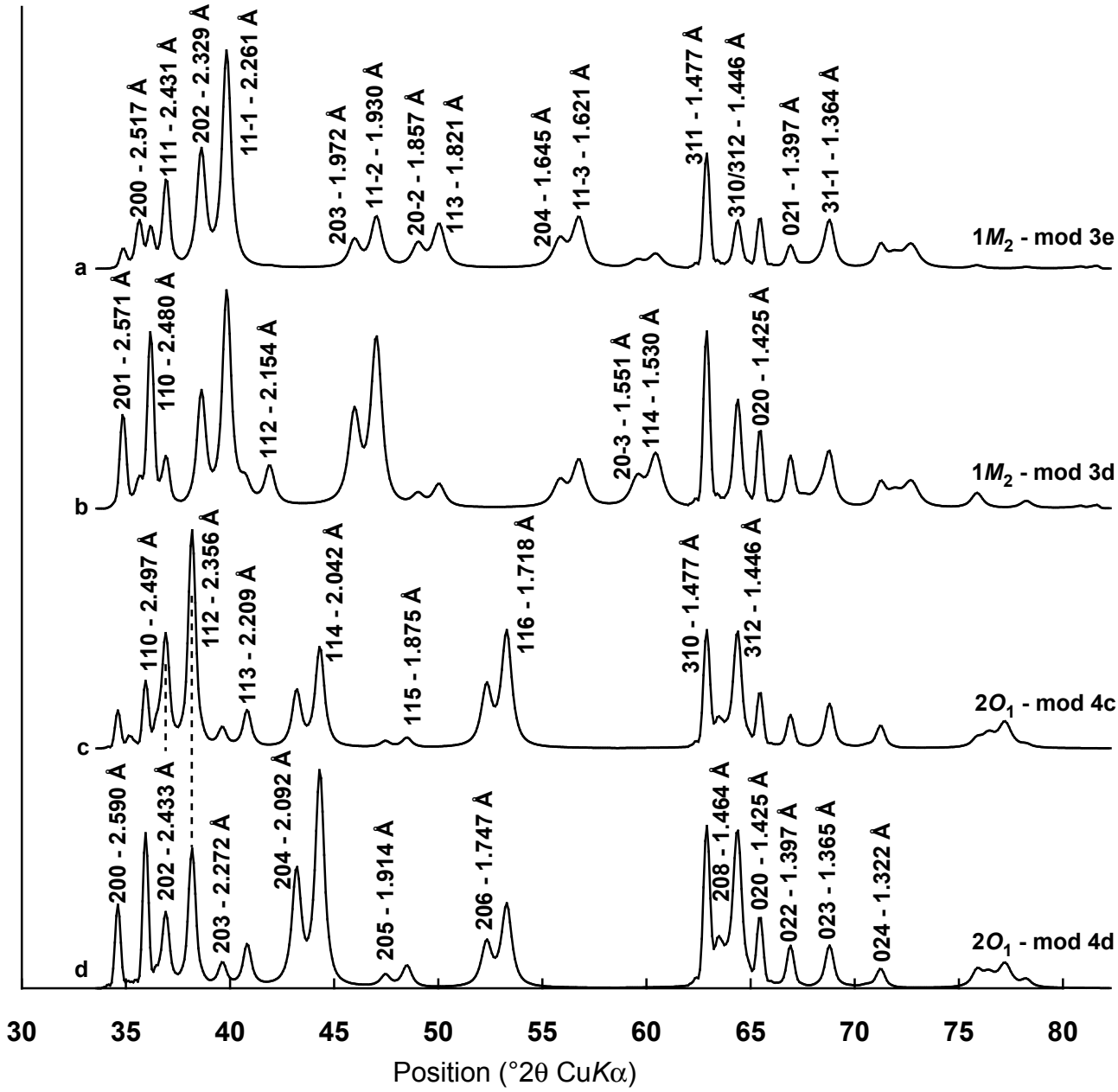

Drits et al. Fig. 07

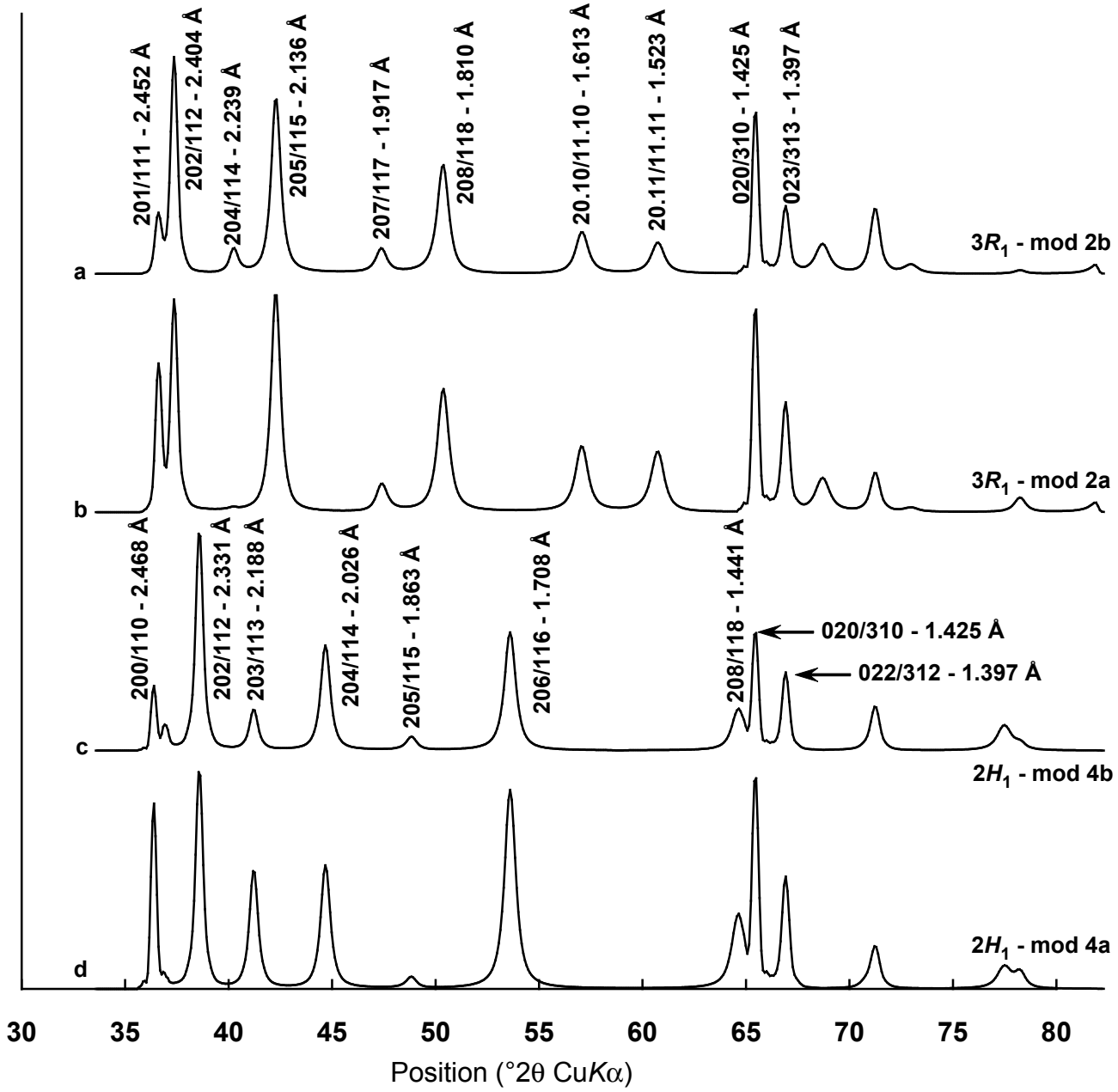

Drits et al. Fig. 08

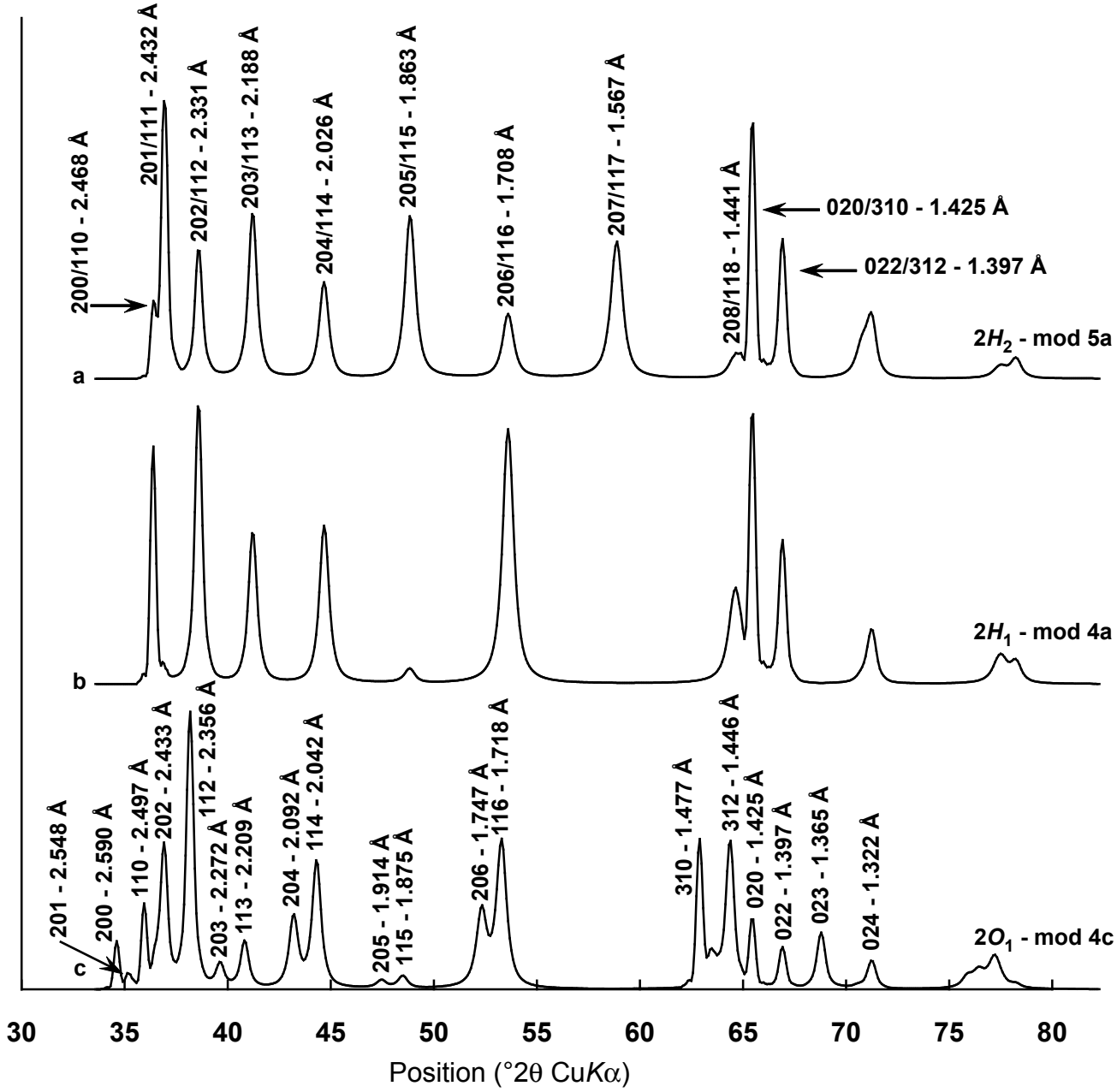

Drits et al. Fig. 09

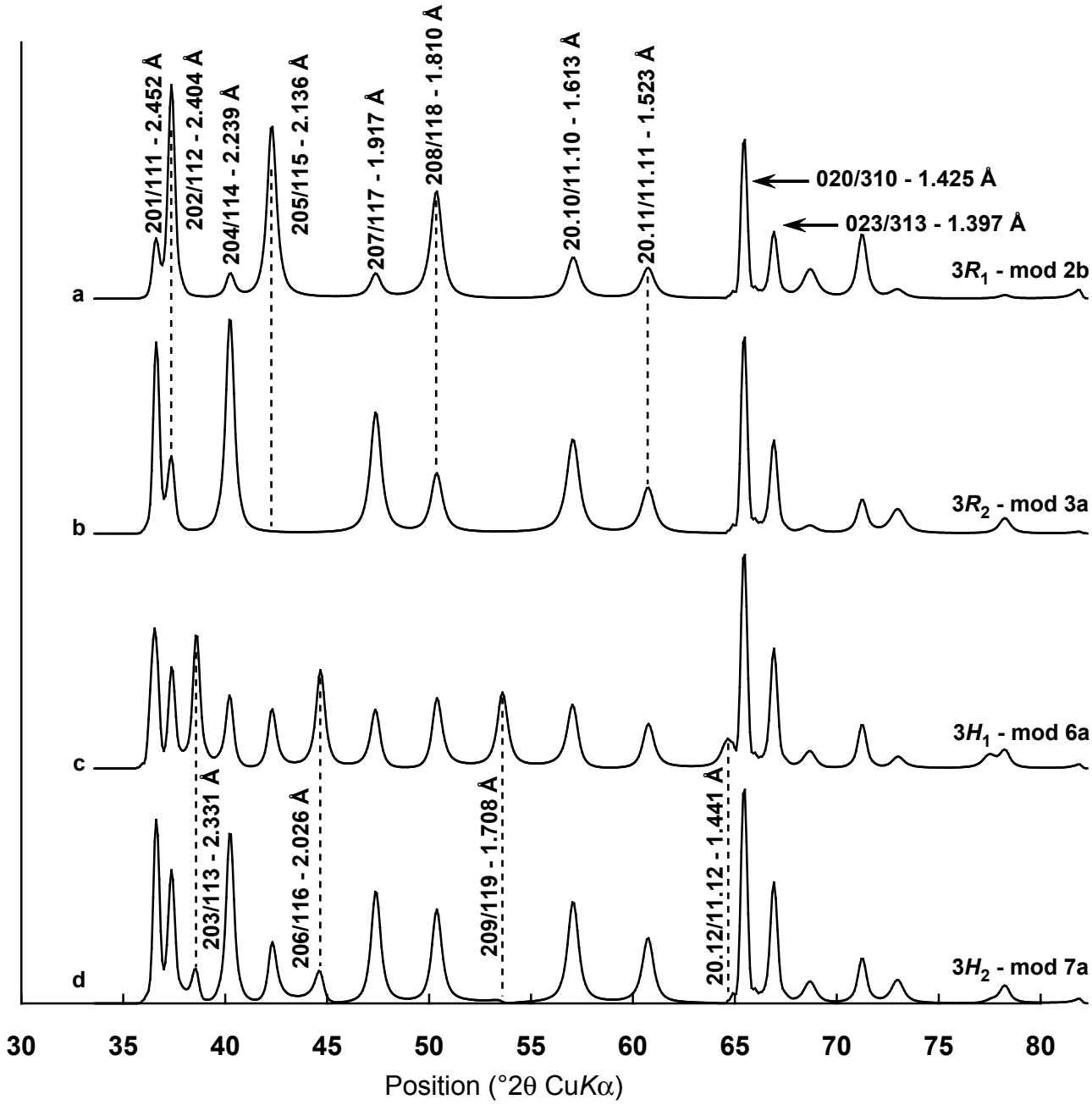

Drits et al. Fig. 10

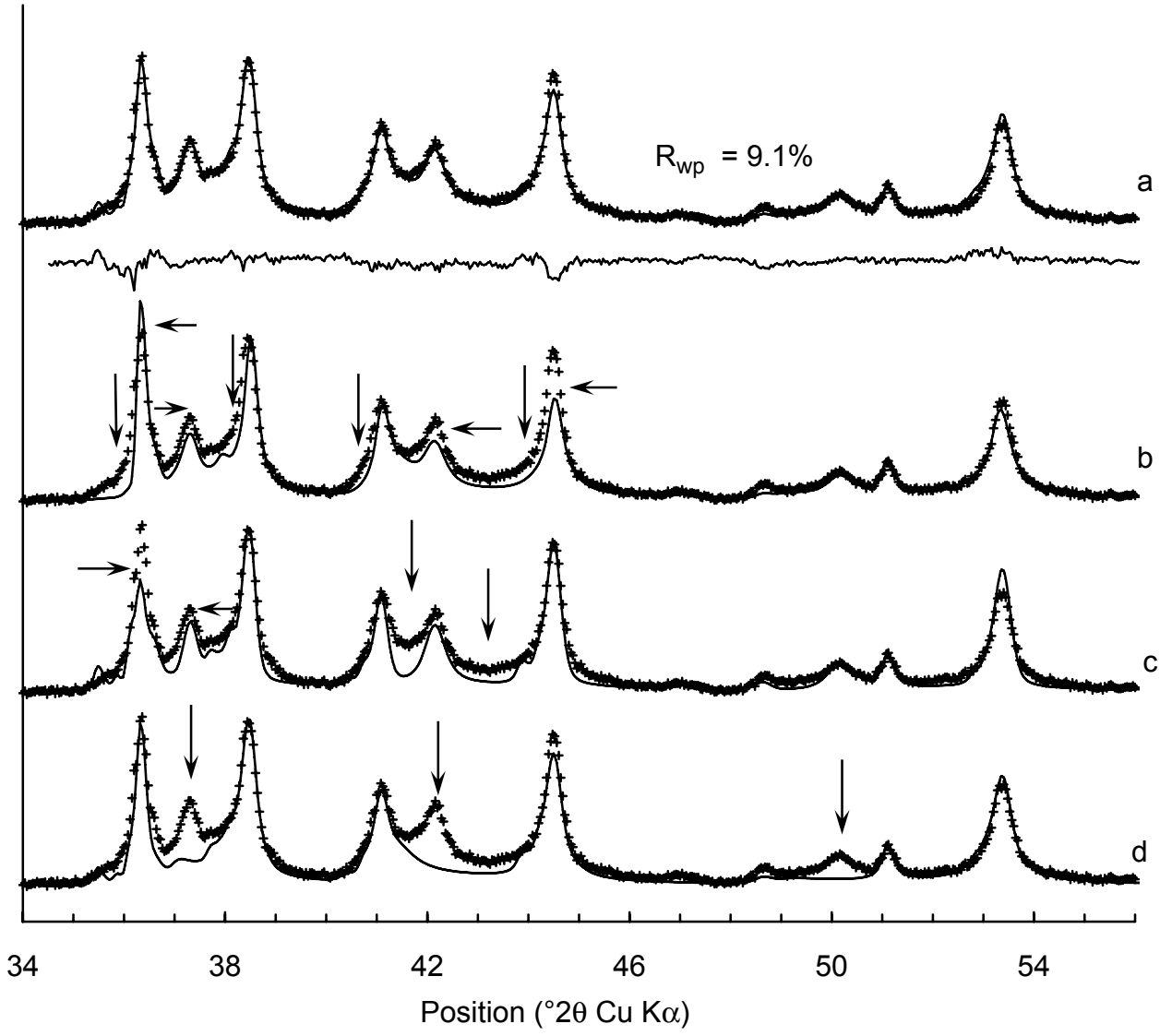

Drits et al. Fig. 11

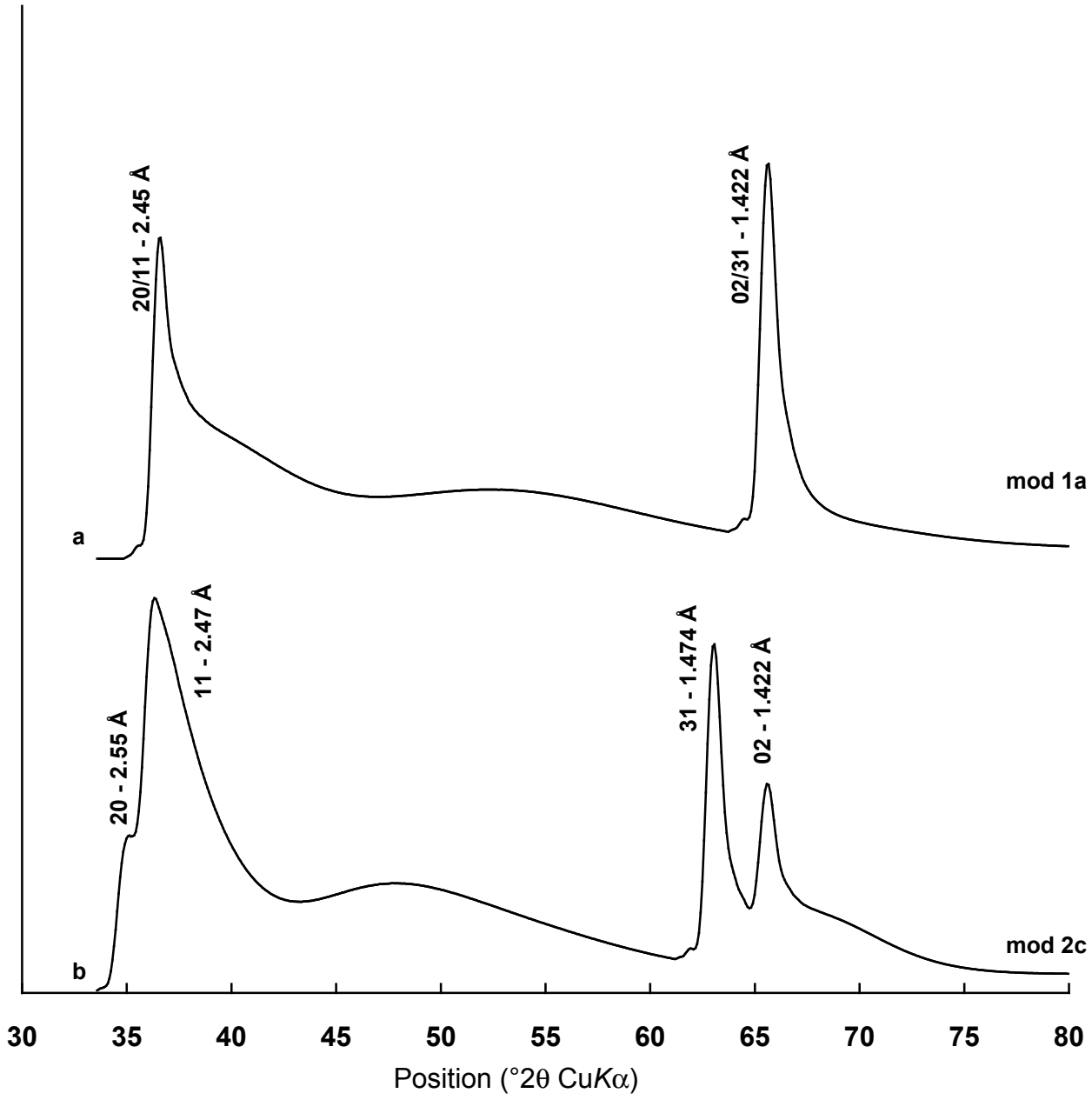

Drits et al. Fig. 12

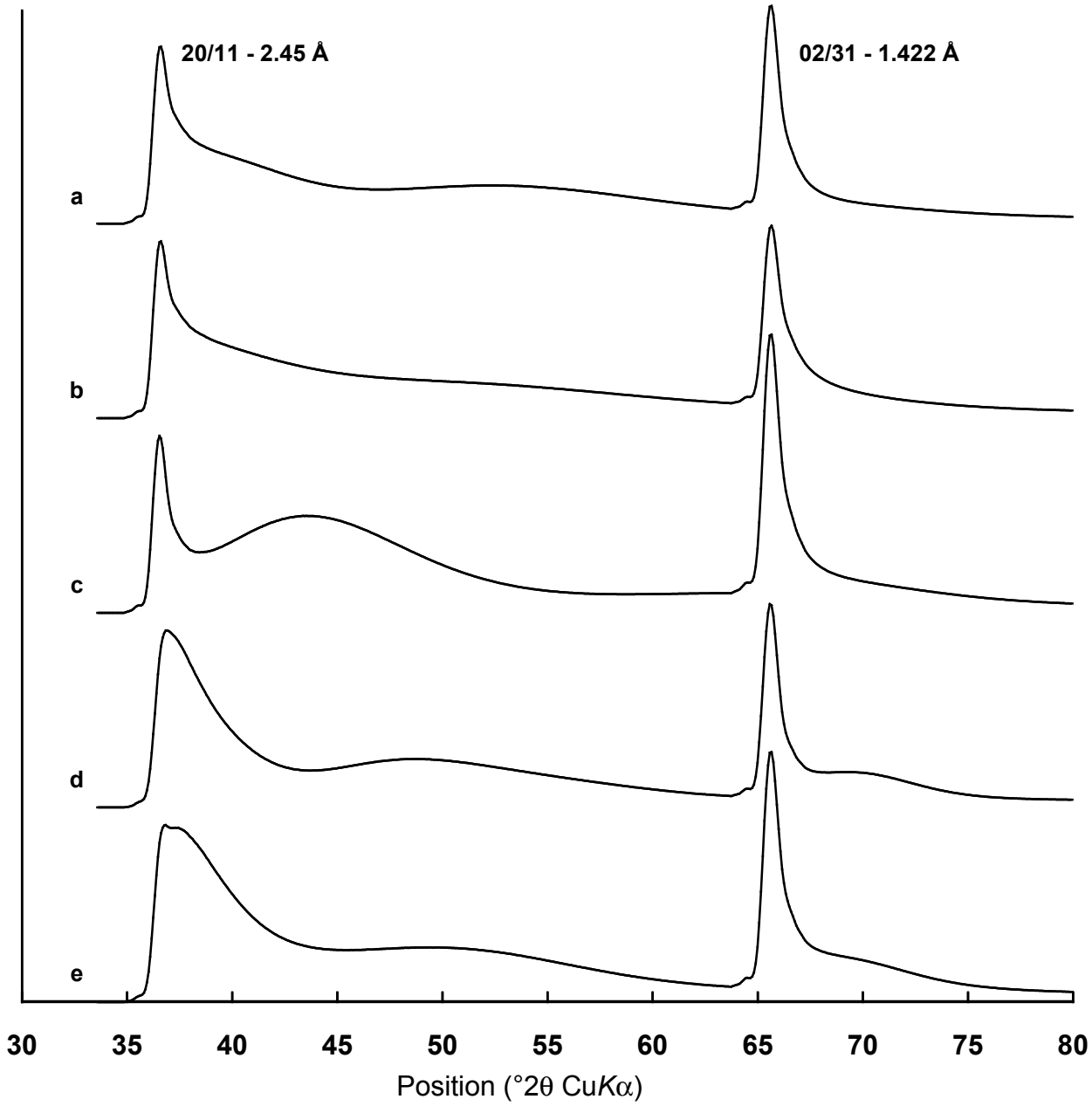

Drits et al. Fig. 13